

2021-12

On the energy conversion characteristics of a top-mounted pitching absorber by using smoothed particle hydrodynamics

Zheng, X

<http://hdl.handle.net/10026.1/18290>

10.1016/j.enconman.2021.114893

Energy Conversion and Management

Elsevier BV

All content in PEARL is protected by copyright law. Author manuscripts are made available in accordance with publisher policies. Please cite only the published version using the details provided on the item record or document. In the absence of an open licence (e.g. Creative Commons), permissions for further reuse of content should be sought from the publisher or author.

On the energy conversion characteristics of a top-mounted pitching absorber by using smoothed particle hydrodynamics

Xiaobo Zheng^a, Guangmao Chen^a, Wenjin Cao^a, Hao Xu^{a,b}, Ruiwen Zhao^a,
Qianlong Xu^a, Morten Kramer^c, David Le Touzé^d, Alistair G.L. Borthwick^{e,f}, Ye
Li^{a,b,g,*}

^a*Lab of Multiple Function Towing Tank, School of Naval Architecture, Ocean & Civil Engineering,
Shanghai Jiao Tong University (SJTU), Shanghai, China*

^b*State Key Lab of Ocean Engineering, SJTU, Shanghai, China*

^c*Department of the Built Environment, Aalborg University, Aalborg, Denmark*

^d*LHEEA Lab, Ecole Centrale Nantes and CNRS, Nantes, France*

^e*School of Engineering, The University of Edinburgh, Edinburgh, UK*

^f*School of Engineering, Computing and Mathematics, University of Plymouth, Plymouth, UK*

^g*Key Lab of Hydrodynamics (Ministry of Education), SJTU, Shanghai, China*

Abstract

The top-mounted pitching point absorber is one of the most promising wave energy converters in that it can be easily attached to an existing offshore structure. However, it is difficult to predict accurately its energy conversion performance because of the strongly nonlinear hydrodynamic behaviour. Herein, smoothed particle hydrodynamics (SPH) is used to solve this wave-structure interaction problem. The SPH method is first validated against free surface deformation measurements obtained from a wedge water entry experiment. SPH simulations of regular wave interaction with fixed and freely pitching devices agree well with measured data, providing confidence in the prediction of power conversion performance. Absorbed power and capture width ratio exhibit uni-modal behaviour with wave period. The wave period of peak power within this distribution increases with PTO damping. According to the observed scaling behaviour with device scale, an optimally damped larger scale device is effective at absorbing energy from incident waves of longer wavelength. In finite deep water, the larger device achieves higher efficiency compared with the smaller ones, and its peak efficiency at $2\pi h/\lambda = 1.1$ provides reference for siting.

Keywords: wave energy conversion, top-mounted pitching point absorber, smoothed particle hydrodynamics, capture width ratio, scale effect

*Corresponding Author: ye.li@sjtu.edu.cn

Nomenclature

Abbreviations

2D two dimensions

3D three dimensions

c-Si PV crystalline silicon photovoltaic cell

CFD computational fluid dynamics

CFL Courant-Friedrichs-Lewy

CWR capture width ratio

NS Navier-Stokes

P1, P2, P3, P4, P5 elevation probe in wave tank

PTO power take-off system

RANS Reynolds-Averaged-Navier-Stokes

RNG renormalised group

RP reference point of wedge-water entry

SPH smoothed particle hydrodynamics

VoF volume of fluid

WEC wave energy converter

Operators

$\bar{\quad}$ mean value

$\sigma(\quad)$ standard deviation value

$\vec{\nabla}$ gradient vector

$||$ magnitude value

Symbols

α	non-dimensional dissipation coefficient in artificial viscosity term
α_D	coefficient in smoothing function
δ	coefficient of density diffusion term
ϵ_x, ϵ_z	relative coordinate discrepancies, %
γ	coefficient in Poisson's equation
Π	artificial viscosity term
λ	wave length, m
λ_I	wave length in water of infinite depth, m
μ	intermediate variable in artificial viscosity term
ρ	fluid density, kg/m ³
ρ_0	reference fluid density, kg/m ³
\vec{F}_d	damping force on PTO, N
\vec{F}_e	excitation force on PTO, N
\vec{g}	acceleration of gravity, m/s ²
\vec{r}	displacement vector between any two given particles
\vec{v}_r	relative velocity of PTO, m/s
\vec{v}	particle velocity, m/s
B	intermediate variable in Poisson's equation
C	linear damping coefficient, Ns/m
c	local sound speed, m/s
c_0	sound speed in water of reference density ρ_0 , m/s
D	diameter of absorber hemispherical bottom, m

F_x, F_z	load components on the float, N
Fr	Froude number
H	wave height, m
h	water depth of wave tank, m
H_d	wedge drop height, m
l	smoothing length
M	PTO mass, kg
m	particle mass, kg
P	absorbed power, w
p	pressure, Pa
P_w	incident power in regular waves, w
q	non-dimensional distance between two particles
Re	Reynolds number
T	wave period, s
t	time, s
W	smoothing function of SPH interpolation
x, y, z	spatial coordinate
X_c	translation of disabled PTO cylinder, m
Z_s	free surface elevation, m

Subscripts

i	the calculated particle
j	a neighbouring particle
n	index of time step
o	optimal damping condition
th	theoretical variable

1. Introduction

Ocean wave energy, an abundant, locally concentrated form of marine renewable energy [1], has received much attention because of its potential benefits for global energy security and environmental protection. Falcão [2] has provided a comprehensive review of different wave energy conversion technologies. According to energy conversion principles, main wave energy converters (WECs) can be classified as overtopping systems [3, 4], oscillating bodies [5, 6], oscillating water columns [7, 8], and membrane devices [9, 10].

1.1. Challenge of wave energy

Over the past few decades, WEC technology has evolved from prototype design towards pilot demonstration devices at ocean test sites. For example, Wave Dragon deployed the world's first offshore grid-connected WEC, an overtopping system, in 2003 [3]. Ocean Power Technologies deployed a 150 kW floating point absorber in 2011 [6]. Oceanlinx deployed a 1/3 scale demonstration device of an oscillating water column in 2010, the tests indicating that a full scale OWC could achieve a rated power of 2.5 MW [8]. Despite their successful operation, these technologies have not yet reached commercialisation because of issues concerning reliability and cost compared with other renewable power sources [11], such as offshore and onshore wind, crystalline-silicon photo voltaic (c-Si PV) and hydro-power (figure 1).

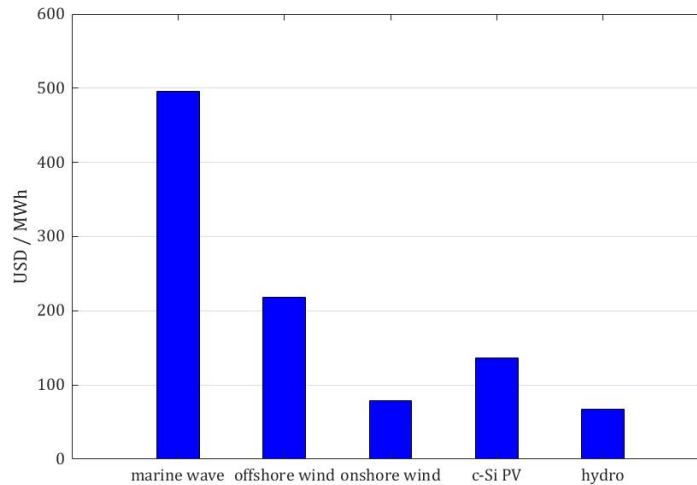


Figure 1: Global levelised cost of renewable energy technologies in 2013 (figure by permission of the World Energy Council, London [12]).

20 Of all the foregoing challenges, cost is the most important, and is mainly affected
 21 by energy conversion efficiency and device scale [13, 14]. Theoretically, the conversion
 22 efficiency from energetic waves per unit volume (usually characterised by capture
 23 width ratio, CWR) is relatively limited [15, 16]. Much research effort on WEC is
 24 therefore directed towards improving conversion efficiency and hence reducing energy
 25 cost. The floating point absorber, a form of oscillating body WEC, is believed to be
 26 one of the most cost-efficient technology by which to extract wave energy [10, 17].
 27 Further to the absorber oscillating in heave, the concept of a pitching point absorber
 28 involves mounting an arm on the top of the absorber with a single pitching degree
 29 of freedom.

30 *1.2. Top-mounted pitching point absorber*

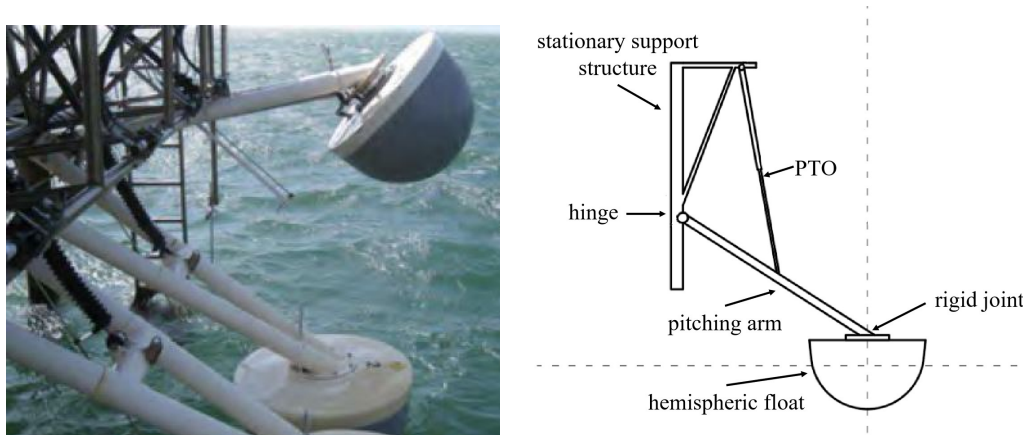


Figure 2: Left: photograph of a Wavestar device deployed at Nissum Bredning, Denmark [18]; right: general concept of top-mounted pitching point absorber.

31 The top-mounted pitching point absorber is designed to work together with other
 32 technologies on an offshore platform [19, 20, 21]. In this way, construction, deploy-
 33 ment, and maintenance costs can be substantially reduced, and so such absorbers of-
 34 fer great potential for deep ocean applications. Perhaps the best known top-mounted
 35 pitching point absorber supplying electricity to the grid is Wavestar [22], which
 36 was first proposed by Niles and Keld Hansen in 2000 [23]. In Wavestar, several
 37 hemispherical-bottomed floats are connected to a stationary support structure with
 38 rigid arms. Each arm is attached at a fixed angle to the top of the float by a rigid
 39 joint. Float motion is constrained to a single rotational degree of freedom about the
 40 hinge point between the stationary support structure and the arm. Wave power is
 41 transformed into mechanical motion of the float and arm, and the power driving this

42 motion is absorbed by means of a hydraulic power take-off system (PTO) connected
43 to an electrical generator that delivers electrical power to the grid. Fig.2 shows a
44 commercial Wavestar device and the general concept of a top-mounted pitching point
45 absorber.

46 *1.3. Numerical studies on the characteristics of point absorbers*

47 In order to improve the efficiency of point absorbers, it is necessary to optimise
48 their hydrodynamic design in the context of wave-structure interaction. Jakobsen et
49 al. [18, 24] carried out experimental studies on top-mounted pitching point absorbers
50 with different float sizes in a wave basin. Jakobsen et al. measured wave and motion
51 induced loads on the absorbers in order to estimate their mean absorbed power, and
52 provided a detailed discussion of the reliability and accuracy of the experiments.
53 Besides experimental tests, numerical studies have proved popular for solving wave-
54 structure interaction problems due to their relatively low cost and accessibility. Li
55 & Yu produced a detailed review of numerical methods for modelling floating-point
56 absorbers [10], including linear potential, empirical prediction, boundary integral
57 equation, and Navier-Stokes (NS) equation methods.

58 Numerical models based on linear potential theory assume inherently that the
59 fluid is inviscid and incompressible, the flow is irrotational, and the amplitudes of
60 wave and device motion are small compared with the device size. Penalba et al. [25]
61 studied the effect of the nonlinear Froude-Krylov force on spherical and cylindrical
62 point absorbers. Jin et al. [26] investigated the effect of nonlinear viscosity on the
63 hydrodynamics of a 1/50 scale point absorber in heave motion. However, actual
64 wave energy devices rarely run under the small-amplitude waves in power absorption
65 mode, for reasons of efficiency. Furthermore, sea wave conditions are ever changing,
66 and strongly nonlinear phenomena such as slamming, crushing, and green water
67 inundation may occur during extreme wave events [27, 28]. Linear potential flow
68 theory performs poorly when applied to such problems [29].

69 Computational fluid dynamics (CFD) based on the NS equations has been widely
70 used to study the hydrodynamics of WECs, which are influenced by strongly nonlin-
71 ear free surface deformation, viscosity, turbulence, and sometimes air compressibil-
72 ity. Yu & Li [30] simulated a two-body floating-point absorber in heave by using the
73 Reynolds-Averaged-Navier-Stokes (RANS) - based finite volume method with the
74 volume of fluid (VoF) interface capture scheme and a $k - \omega$ Shear Stress Transport
75 turbulence model. They analysed the hydrodynamic response and energy conversion
76 in regular waves, and demonstrated the significance of the nonlinear effects for the
77 power output in the case of heaving point absorber under large steepness waves.
78 Ransley et al. [31] reviewed existing CFD simulations in which the motion of a

79 moving structure is calculated by considering fluid-structure interaction, and then
80 developed a fully nonlinear and coupled tool using the RANS-VoF method and the
81 renormalised group (RNG) $k - \epsilon$ turbulence model. They simulated hydrodynamics
82 of the 1/10 scale Wavestar device in regular waves of varied steepness, and found
83 the numerical results compare well with measurements by Jakobsen et al. [24]. The
84 RANS models in the Eulerian framework require high resolution meshes. To re-
85 solve wave-structure interaction at high accuracy, Eulerian methods also need an
86 additional interface precise capturing scheme. Furthermore, strongly nonlinear wave
87 phenomena, such as slamming, crushing, and green water inundation, commonly oc-
88 cur at the free surface. When there is an additional fluid-structure interaction with a
89 floating device, modelling of such nonlinear processes requires mesh reconstructions
90 that can handle grid distortion, making the computation even more complicated
91 [32, 33]. Conversely, Lagrangian particle methods are meshless, which is a key fea-
92 ture in the cases where the free-surface experiences large deformation. Among the
93 Lagrangian particle methods, smoothed particle hydrodynamics (SPH) has become
94 the most popular.

95 Since its original development by Gingold & Monaghan [34] and Lucy [35] in
96 1977 for applications in astrophysics, SPH has proved applicable to a wide range of
97 fluid flow problems including, e.g., gas bubble dynamics [36], water wave generation
98 and propagation [37], and fluid-structure interaction [38, 39, 40, 41, 42]. Shadloo
99 et al. [43] reviewed applications of the SPH method in engineering fields, such as
100 aerospace, transportation, environment, geophysics, and energy production. They
101 summarised the motivations behind utilising the SPH method in an industrial con-
102 text, and derived general conclusions regarding its assets and limitations. Compared
103 with mesh-based Eulerian methods, SPH modelling uses interpolation functions to
104 calculate spatial quantities and their derivatives from an arbitrary set of calculation
105 points, giving it the meshless nature. This method naturally incorporates disconti-
106 nities across the interface and singular forces into the numerical scheme, and does
107 not need special treatment to detect the free surface and different phases in space
108 [33]. It also preserves perfectly sharp interfaces between phases, even in case of large
109 deformation of the free surface or air entrapment in the water. Finally, it directly
110 models moving complex interfaces and boundaries due to its Lagrangian nature, giv-
111 ing remarkable advantages regarding free surface flow simulation and wave-structure
112 interaction analysis. Therefore, for wave energy utilisation, SPH serves as a promis-
113 ing tool to capture the violent hydrodynamics of waves that break, run up, overtop
114 and interact with WECs, see, e.g., [44, 45, 46, 47, 48].

115 1.4. Research Objectives

116 In order to balance the power capture efficiency, cost, and security of top-mounted
117 pitching point absorbers, a deep understanding is required of the characteristics of
118 energy conversion and associated hydrodynamics. Without loss of generality, we
119 apply the geometry of Wavestar to study energy conversion performance by alter-
120 ing the incident wave condition and PTO damping coefficients. Particular attention
121 is given to the effect of float scale on absorbed power by optimised PTO. In this
122 study, the SPH method is used to solve the wave-structure interaction problem be-
123 cause of its inherent accuracy in capturing violent free surface deformation. More
124 specifically, Section 2 outlines the numerical model based on the SPH method, fol-
125 lowed by validation of its capability to accurately capture complex free surface flow.
126 Section 3 compares the hydrodynamics of the wave-device interactions simulated by
127 the SPH method with experimental data and alternative RANS predictions. Section
128 4 discusses the effects of wave height, wave period, PTO damping coefficient, and
129 device scale on absorbed power and capture width ratio. Section 5 examines opti-
130 mal absorbed power by considering the effects of scale and water depth. Section 6
131 summarizes the main conclusions.

132 2. Numerical method

133 2.1. SPH method

134 In SPH modelling, the fluid domain volume is discretised into a set of elementary
135 fluid volumes called particles. Spatial differential operators involved in the evolu-
136 tion equations of the system, e.g. the Navier-Stokes equations, are computed by
137 interpolation from neighbouring particles within a characteristic distance called the
138 smoothing length. The contribution of these neighbour particles depends on the
139 distance between particles and a weighted kernel function of compact support. The
140 main steps of an SPH algorithm are as follows [49]: i) neighbouring particles are first
141 searched using a linked-list algorithm [50] (for efficiency this list can be kept for a
142 number of time steps using a slightly larger neighbourhood); ii) governing equations
143 and boundary conditions are then solved with involved spatial differential operators
144 estimated through the aforementioned interpolation; iii) particle quantities are up-
145 dated using standard or symplectic time integration schemes. In the present work,
146 a standard weakly compressible SPH model is used to solve the fully coupled prob-
147 lem of wave-WEC interactions with the open source software package DualSPHysics
148 (<https://dual.sphysics.org>).

149 The weighted kernel function of the aforementioned SPH interpolation, also called
150 smoothing function, is noted by W . In the present work a quintic spline [51] is used

151 which can be written as a function of the non-dimensional distance q as [52, 53]:

$$W(q) = \alpha_D \left(1 - \frac{q}{2}\right)^4 (2q + 1), 0 \leq q \leq 2, \quad (1)$$

152 where α_D is $7/4\pi l^2$ in two dimensions (2D) and $21/16\pi l^3$ in three dimensions (3D).
 153 $q = |\vec{r}|/l$, where \vec{r} is the displacement vector between any two given particles and
 154 l the smoothing length. The SPH method used herein assumes the fluid is weakly
 155 compressible. Pressure is calculated from the equation of state, which is more efficient
 156 and easier for parallel computing than by Poisson's equation [54]:

$$p = B \left[\left(\frac{\rho}{\rho_0}\right)^\gamma - 1 \right], \quad (2)$$

157 where p is pressure, ρ is fluid density, $\gamma = 7$, and $B = c_0^2 \rho_0 / \gamma$. Another essential
 158 feature of the weakly-compressible version of SPH compared to the incompressible
 159 version is that no free-surface detection is needed to impose free-surface boundary
 160 conditions in case of single-phase free-surface simulation [55, 56]. $c(\rho) = \sqrt{\partial p / \partial \rho}$
 161 is the local sound speed, and $c_0 = c(\rho_0)$ is the speed of sound in water of reference
 162 density ρ_0 . For computational efficiency, under the weak-compressibility assumption
 163 an artificially low value is used for c_0 so that fluid compressibility is limited to within
 164 1% about the reference density $\rho_0 = 1000 \text{ kg/m}^3$ for water.

165 In the used DualSPHysics package the discrete SPH continuity and momentum
 166 equations are expressed as [53]:

$$\frac{d\rho_i}{dt} = \sum_j m_j \vec{v}_{ij} \cdot \vec{\nabla}_i W_{ij} + 2\delta l c_0 \sum_j (\rho_j - \rho_i) \frac{\vec{r}_{ij} \cdot \vec{\nabla}_i W_{ij}}{|\vec{r}_{ij}|^2} \frac{m_j}{\rho_j}, \quad (3)$$

167 and

$$\frac{d\vec{v}_i}{dt} = - \sum_j m_j \left(\frac{p_j + p_i}{\rho_j \rho_i} + \Pi_{ij} \right) \vec{\nabla}_i W_{ij} + \vec{g}_i, \quad (4)$$

168 where m is particle mass, \vec{v} is particle velocity, and \vec{g} is acceleration of gravity.
 169 Subscripts i and j indicate the calculated particle and a neighbouring particle re-
 170 spectively, thus $\vec{v}_{ij} = \vec{v}_i - \vec{v}_j$ and $\vec{r}_{ij} = \vec{r}_i - \vec{r}_j$. In standard (fully-Lagrangian) SPH
 171 simulations, the mass of each fluid particle remains constant so that the density can
 172 be not explicitly involved in the first term on the right side of the continuity equation
 173 [52]. In addition, following Molteni & Colagrossi [57] a density diffusion term with
 174 $\delta = 0.1$ is added in the continuity equation to reduce density fluctuations in the sim-
 175 ulations. Note that more sophisticated form of this density diffusion term was later

176 proposed by Antuono et al. [58]. In the momentum equation, the symmetric form of
 177 plus pressure discretization [59] is utilised for the conservation of linear and angular
 178 momenta in the particle system. Considering the required accuracy [37, 40, 45] and
 179 computational costs, the simple artificial viscosity model is adopted in the momen-
 180 tum equation instead of other more accurate models [60]. The common form of the
 181 artificial viscosity term Π is written as,

$$\Pi_{ij} = \begin{cases} -\frac{\alpha \bar{c}_{ij} \mu_{ij}}{\rho_{ij}}, & \vec{v}_{ij} \vec{r}_{ij} \leq 0, \\ 0, & \vec{v}_{ij} \vec{r}_{ij} > 0, \end{cases} \quad (5)$$

182 where $\mu_{ij} = l \vec{v}_{ij} \vec{r}_{ij} / (r_{ij}^2 + 0.01l^2)$, $\bar{c}_{ij} = (c_i + c_j)/2$, and $\rho_{ij} = (\rho_i + \rho_j)/2$. α is the
 183 non-dimensional dissipation coefficient with a positive value, which is chosen as small
 184 as possible to avoid excessive dissipation for violent-dynamic flows. In the present
 185 study, $\alpha = 0.01$ is found to be a good choice to avoid excessive dissipation [37] and
 186 to improve the numerical stability [39]. Note that since no physical viscosity term
 187 is discretized and the artificial viscosity term tends to zero with particle refinement,
 188 the momentum equation is essentially an Euler equation, which is an appropriate
 189 choice for the targeted application.

190 A numerically stable explicit second-order symplectic method is used as the time
 191 integration scheme. This method is with a time accuracy of $O(\Delta t^2)$ and involves
 192 predictor and corrector stages. A variable time step criterion [61] is used within the
 193 time integration, i.e., the time step is dependent on the Courant-Friedrichs-Lewy
 194 (CFL) condition, the mass force term and the viscous diffusion term. The speed
 195 of sound, mass force and viscosity force are calculated for all particles at each time
 196 step, which in turn determines the size of the next time step with the value of the
 197 CFL number adopted as 0.2.

198 In the present single phase SPH modelling, the free surface is identified by search-
 199 ing for the interpolated nodal mass larger than a given reference mass which is set as
 200 half the fluid mass in 3D [53]. The SPH model naturally incorporates discontinuities
 201 across the interface into the numerical scheme. Therefore, no other special treatment
 202 is needed as mesh-based Eulerian methods [33]. A shifting algorithm is used in the
 203 DualSPHysics model. This algorithm addresses the instability issue of anisotropic
 204 particle spacing in the violent fluid-structure-interaction cases, and eliminates noises
 205 in the velocity, density and pressure fields caused by the instability [62].

206 Solid objects in the SPH modelling are assumed rigid. The dynamic impermeable
 207 and free-slip boundary condition is implemented for solid boundaries of rigid objects.
 208 In the used DualSPHysics model, the solid boundary is described as a separate set of
 209 particles to the fluid particles. Solid boundary particles satisfy the same equations
 210 as fluid particles. The solid objects are classified as the fixed objects (e.g. tank

211 walls and fixed float), the motion-determined object (e.g. wave maker), and the
212 fluid-driven objects (e.g. water-entry wedge and pitching float). These three types
213 of solid objects are differently treated. On the fixed objects, boundary particles
214 remain fixed in position. The paths of boundary particles on motion-determined
215 objects are calculated from an imposed motion function (Dalrymple & Knio [63]). In
216 contrast, the movement of boundary particles on fluid-driven rigid objects is derived
217 by considering the interaction with neighbouring fluid particles (Crespo et al. [64]).
218 If a fluid particle approaches any solid boundary and the distance between solid and
219 fluid particles becomes smaller than twice the smoothing length, the density of the
220 boundary particles becomes larger, causing a pressure increase. This results in a
221 repulsive force being exerted on the fluid particle due to the pressure term in the
222 momentum equation. The net force on each boundary particle is the summation
223 of the contributions from all surrounding fluid particles according to the designated
224 kernel function and smoothing length. The force exerted by fluids onto a solid object
225 is calculated as the summation of the net force of each solid boundary particle.
226 Furthermore, considering the calculated hydrodynamic force by fluids, the gravity
227 and the existing constraints, the movements of the fluid-driven object and hence of
228 the boundary particles are achieved by time integration [64]. The interaction between
229 solid objects with different restrictions (e.g., hinges and springs) is solved by using
230 the open source multiphysics simulation engine Project Chrono [65].

231 *2.2. Validation of complex free surface deformation*

232 In order to provide validation data for verifying the capability of the SPH model
233 to simulate violent fluid-structure interaction problems, experimental tests were car-
234 ried out on the entry of a 2D wedge into a tank of water. Unlike tests on a point
235 absorber in a water basin by Jakobsen et al. [24], which studied the loading on the
236 moving body, the present experiment focuses on deformation of the water free sur-
237 face. Simulation accuracy is then estimated by quantifying the discrepancy between
238 the predicted and experimental free surface deformation. SPH model performance
239 is checked for a series of extreme events that occur during wedge entry including
240 slamming, green water inundation, splashing, break-up, and recombination.

241 *2.2.1. Experimental setup*

242 The experiment was conducted in a water flume of length 1 m, width 0.35 m
243 and still water depth 1 m. The wedge was 0.3 m long, with triangular cross-section
244 of width 0.1 m and deadrise angle of 30 degrees. The mass of the wedge was 4 kg.
245 An aluminium alloy frame was use to attach the wedge. The width of the flume
246 and the length of the wedge had similar dimensions. In order to suppress water

247 splash from the ends of the wedge and to make the water entry an approximately 2D
 248 phenomenon, the flume width and the wedge length were aligned by a laser aligner,
 249 which provided a laser sheet of 2 mm thickness. To ensure single-degree-of-freedom
 250 wedge motion in the vertical direction, two parallel vertical guide rods and four ball
 251 bearings were used. The vertical rods were fixed to the top of the wedge, which
 252 were also checked by the laser aligner with the direction deviation less than 3 degree.
 253 The friction coefficient of ball bearings was 0.001, causing negligible frictions and
 254 approximately free fall motion for the dropping wedge.

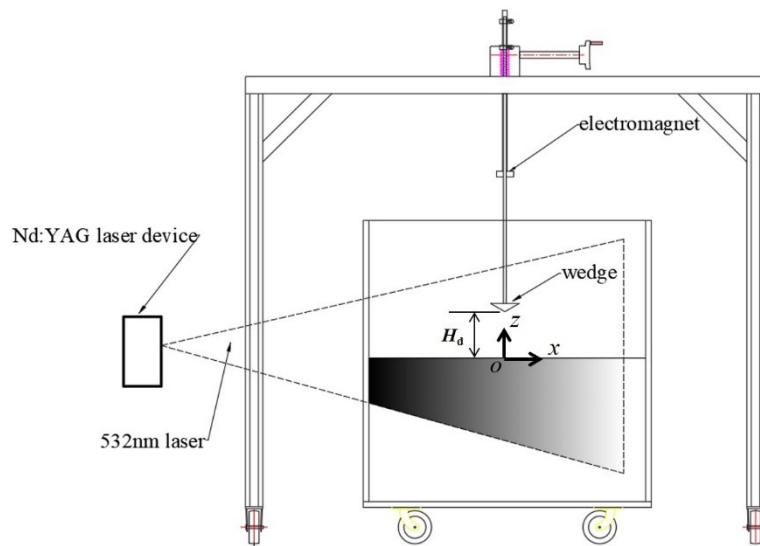


Figure 3: Schematic showing setup of 2D wedge-water entry experiment.

255 The drop height of the wedge H_d was adjusted by using a traverse system with
 256 a resolution of 0.5 mm. The start time of the dropping was controlled by an elec-
 257 tromagnetic switch. An Nd:YAG laser was operated in continuous mode with a
 258 constant power output of 6 W to provide a 532 nm laser sheet. The area of in-
 259 terest on the mid-wedge-length plane was illuminated, ensuring the 2D profiles of
 260 free surface captured. Water entry by the wedge was monitored by a high-speed
 261 CMOS camera, Phantom Miro eX4, with a frame rate of 1000 fps and resolution
 262 of 800×600 pixels. An optical filter was attached on the camera lens to suppress
 263 image noises from external light fields. Fig.3 shows the experimental setup with the
 264 (x, z) coordinate system defined with the origin at the point of wedge entry to the
 265 water. Here, x is in the horizontal (right positive) direction, and z is in the vertical
 266 (upwards) direction.

267 *2.2.2. Comparison between simulated and experimental results*

268 In the experiments, the evolving interfaces between water, air, and wedge dur-
 269 ing the entry process were all captured. Fig.4 compares SPH model simulated free
 270 surface profiles (in the foreground) throughout the splash stage with experimental
 271 measurements (in the background) for cases with drop heights $H_d = 0.05$ and 0.10
 272 m at time instants $t = 0.050$ and 0.136 s after the wedge first contacts the otherwise
 273 still water surface.

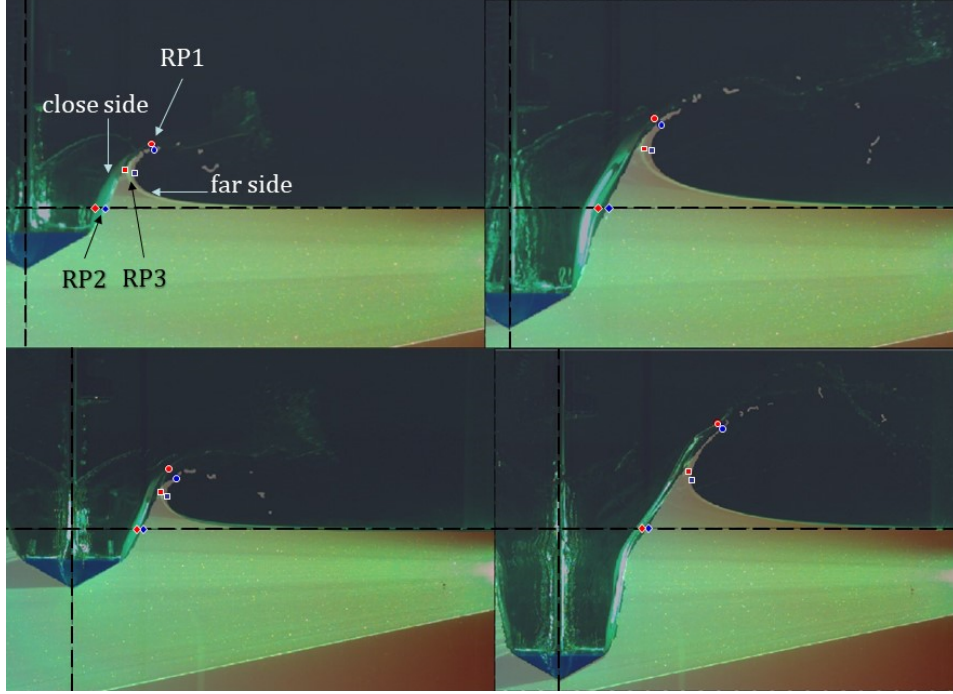


Figure 4: Comparison of free surface deformation profile and reference points (RP1: circle; RP2: square; RP3: diamond) between experiment (background contour and red symbol) and SPH simulation (foreground contour and blue symbol). Horizontal and vertical dashed lines: still water level and wedge dropping trajectory. Top: $H_d = 0.05$ m; bottom: $H_d = 0.10$ m. Left: $t = 0.050$ s; right: $t = 0.136$ s.

274 For $H_d = 0.05$ m, the free surface deforms at the sides of the wedge at $t = 0.050$ s
 275 with a plunging water jet evident. At $t = 0.136$ s, the jet flow is more developed with
 276 an obvious increase in magnitude of free surface deformation. Compared with the
 277 free surface impacted by the wedge in the experiment, the simulated surface has less
 278 curvature and the jet splash is slightly weaker, partly because of the relatively large
 279 size of the SPH particles [41] and lack of surface tension in the theoretical model.

280 Both the entry velocity and slamming force increase with increased drop height.

281 Compared with the results for the $H_d = 0.05$ m case, the free surface profile close to
 282 the wedge for $H_d = 0.10$ m becomes straighter and the peak of the continuous free
 283 surface occurs further from the tip of the wedge under the larger slamming force.
 284 Moreover, the jet splash is larger and does not collapse so quickly onto the otherwise
 285 calm water surface. The variations in free surface deformation and jet splash due to
 286 changing H_d are properly captured by the SPH simulation.

287 Furthermore, three reference points on the $x - z$ plane are selected to give a quan-
 288 titative estimate of the discrepancy between the SPH prediction and experimental
 289 measurement. The first reference point (RP1, circle symbol) is the peak of the con-
 290 tinuous free surface. The second one (RP2, square symbol) is at still water level (i.e.
 291 the horizontal dashed line) on the close side. The third one (RP3, diamond symbol)
 292 is the closest to the wedge dropping trajectory (i.e. the vertical dashed lines) on the
 293 far side. The reference points from measurements and simulations are respectively
 294 marked in red and blue. Here, we define the relative coordinate discrepancy ϵ_x and
 295 ϵ_z as the difference of the coordinate values of a simulated reference point from the
 296 coordinate values of a corresponding measured reference point divided by the wedge
 297 width. Table 1 lists the relative coordinate discrepancies ϵ_x and ϵ_z for three refer-
 298 ence points. Although no quantitative reference could be found from other numerical
 299 studies for comparison purposes, the present relative deviation ($< 17\%$) is satisfac-
 300 tory in terms of capturing the free surface deformation in this wedge water entry
 301 problem. The present SPH model is therefore verified by accurately reproducing the
 302 free surface in the violent water-structure interactions.

Table 1: Relative coordinate deviations between simulated and measured reference points.

H_d , m	t , s	RP1		RP2		RP3	
		ϵ_x , %	ϵ_z , %	ϵ_x , %	ϵ_z , %	ϵ_x , %	ϵ_z , %
0.05	0.050	5.0	-8.3	13.3	0	15.0	-6.7
	0.136	12.7	-12.7	16.4	0	14.5	-3.6
0.10	0.050	14.0	-16.0	12.0	0	12.0	-12.0
	0.136	8.9	-11.1	13.3	0	8.9	-15.6

303 3. Hydrodynamic Modelling of the scaled device

304 We now simulate the hydrodynamics of a top-mounted pitching point absorber
 305 with a hemispherical-bottomed float in order to validate the SPH model for a more
 306 complicated wave-structure problem.

307 *3.1. Model setup*

308 The present NWT has dimensions corresponding to the test tank considered
309 in experimental work by Jakobsen et al. [24], as shown in the top panel of fig.5.
310 Jakobsen et al. carried out large-scale experiments on a 1/10 scale model in the
311 COAST Ocean Basin of the University of Plymouth, UK, and obtained measurements
312 of wave elevation and motion-induced loads in regular waves as well as under extreme
313 conditions. In addition, Ransley et al. [31] reproduced regular wave interactions
314 with both a fixed and a freely-pitching 1/10 scale model using a RANS-VoF method
315 with the RNG $k - \epsilon$ turbulence model. With permission from Jacobsen et al., their
316 experimental data are utilised to validate the present SPH model, and the alternative
317 numerical results by Ransley et al. used for comparison purposes.

318 In the SPH simulation for validation, the computational domain is 16 m long
319 and 6 m wide with a wave maker and a wave absorber situated at the upwave and
320 downwave boundaries respectively. The water depth h is 3 m. The middle and lower
321 panels of fig.5 depict the NWT and device model. The total height of the 1/10 scale
322 float is 0.72 m, and the diameter of the hemispherical bottom is $D = 1$ m. Below
323 we use the hemisphere diameter D as the referential size of the scaled device. The
324 Cartesian coordinate system is defined by the right-hand rule with the origin located
325 at the still water surface close to the wave maker, the x ordinate directed in the
326 horizontal wave propagation direction, and the z ordinate directed upwards in the
327 vertical direction.

328 A piston type wave maker is used to produce regular long-crested waves. Ac-
329 cording to a transfer function, the displacement of the piston is calculated from the
330 desired free surface elevation. The transfer function of a second-order Stokes theory
331 proposed by Madsen [66] is adopted, preventing the generation of spurious secondary
332 waves. The produced waves will not change shape as they propagate, and are ab-
333 sorbed by a passive damping zone with a quadratic decay function [37]. Table 2 lists
334 the wave properties produced in the NWT, including the wave period T and the wave
335 height H . In the SPH model, nearly 2 million particles are generated with particle
336 size of 0.05 m. Owing to the Lagrangian nature of the SPH method and to its al-
337 ready mentioned property of intrinsically verifying free-surface boundary conditions,
338 the air phase effect can be neglected and then the complex single-phase free-surface
339 motion prediction does not require any special treatment.

340 The scaled device is constrained to pitch about an axis passing through the hinge
341 point which connects the stationary support structure and the device arm. The other
342 end of the arm is attached to the hemispherical-bottomed float. The scaled device
343 is initially located at the neutrally-buoyant position with the hemispherical bottom
344 centred at $x = 5.0$ m, $y = 0$ and $z = 0.1$ m. The draught of the float is 0.4 m and

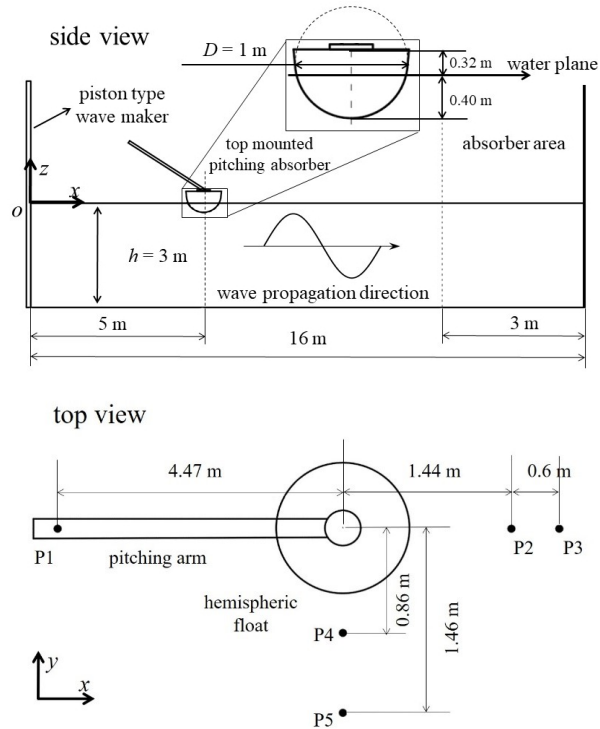
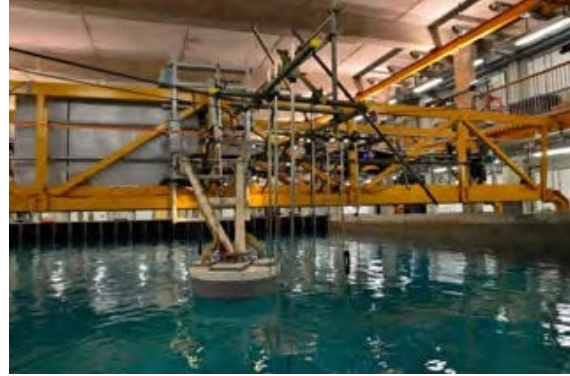


Figure 5: Top: picture of experimental setup in the Ocean Wave Basin at the University of Plymouth, UK [24]; middle: SPH numerical model of the scaled device and NWT from side view; bottom: wave probes used for surface elevation measurements for fixed device from top view.

345 the water-plane diameter is 0.98 m. The mass of the scaled device is 220 kg centred
 346 at $dx = 1.4$ m, $dy = 0$ and $dz = -1.3$ m relative to the pitching axis. The moment
 347 of inertia for pitch motion is $124.26 \text{ kg} \cdot \text{m}^2$. The natural period of the model with
 348 $D = 1$ m is about 1.9 s according to the free decay test of the present SPH simulation

Table 2: Regular wave test parameters.

	D , m	h , m	T , s	H , m	reported in
Scale 1	1	3	2.8	0.25	Section 3
	1	3	2.0	0.68	
Scale 1	1	3	1 - 6	0.25,2	Section 4
Scale 2	5	15	4 - 12	2	
Scale 3	10	30	9 - 21	2	

349 and the measurement by Jakobsen et al. [24].

350 3.2. Comparison with experimental results

351 Three cases are simulated, one for a fixed pitching scaled device, the other two
352 for a freely pitching scaled device. We first consider regular waves with $H = 0.25$ m
353 and $T = 2.8$ s, and then consider extreme waves with $H = 0.68$ m and $T = 2.0$ s (see
354 table 2). In these cases, the same NWT, device geometry and initial position of the
355 float (the neutrally-buoyant position) are considered. Note that the complexity of
356 the simulation increases for the freely pitching device owing to the coupled motion
357 of the float, compared with the fixed device. The complexity further increases for
358 the extreme waves owing to the large-amplitude kinematics and strong nonlinear
359 phenomena such as green water and slamming, compared with the small-steepness
360 waves. However, all the execution times for hydrodynamic simulations of 18 s in
361 three cases are about 22.5 h, running on one Intel® Core™ i7-7700HQ CPU @ 2.80
362 GHz processor (4 cores and 8 threads) and NVIDIA GeForce GTX 1060 GPU. In
363 contrast, the computational cost is found to increase significantly due to the moving
364 mesh and the large-deformation mesh in RANS-VoF simulations by Ransley et al.
365 [31]. The limited computational cost of simulating fluid-structure-coupled kinematics
366 and large-steepness waves is one of the advantages of the meshless SPH method over
367 the mesh-based RANS-VoF method.

368 3.2.1. Fixed device

369 In the fixed case, the model is locked at the neutrally-buoyant position throughout
370 the simulation. Five wave probes monitor the surface elevations, as shown in the
371 bottom panel of fig.5: P1 is positioned close to the wave maker (4.47 m upstream of
372 the float centre), P2 and P3 are downstream of the float centre by 1.44 m and 2.04
373 m, and P4 and P5 are 0.86 m and 1.46 m from the float centre along the wave crest.

374

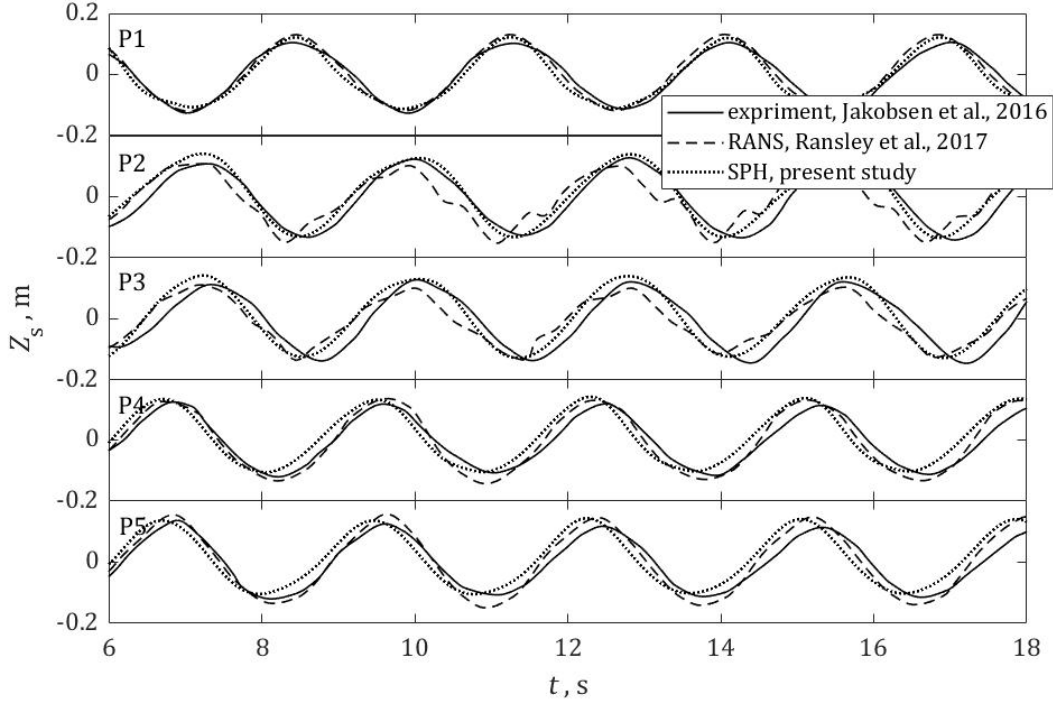


Figure 6: Surface elevation time histories at five probe locations surrounding the fixed device with $D = 1$ m in regular waves of height $H = 0.25$ m and period $T = 2.8$ s.

375 Fig.6 and fig.7 compare the SPH predictions of surface elevation Z_s and load
 376 components on the device model F_x and F_z with the measurements by Jakobsen et
 377 al. [24]. In order to allow initial transients to decay, we only consider numerical
 378 and experimental results after 6 s (about 2 wave cycles and 33% of total simulation
 379 duration) have occurred once wave generation has been initiated.

380 The results at P1 in fig.6 show that the incident wave is reproduced well, with
 381 an amplitude over-estimate of about 2.3% which is smaller than the over-estimate of
 382 10.1% obtained by Ransley et al. [31] using a RANS-VoF model. This suggests that
 383 the present SPH method is more accurate than RANS-VoF at reproducing the wave
 384 surface behaviour. This also provides confidence in the particle resolution given that
 385 there are only 5 acceptable particles over the height of the wave.

386 The results at P2 and P3 in fig.6 show the surface elevation motions with time
 387 in the wake region of the float. It can be seen that the presence of the float does
 388 not significantly disturb the free surface downstream. Compared with the RANS

389 simulation which predicts a high frequency disturbance to the waveform, the SPH
390 simulation gives a smoother representation of the temporal evolution of the surface
391 elevation as would be expected close to the wave maker. The crests simulated by
392 the SPH model are slightly larger than the experimental ones, whereas the troughs
393 are smaller, leading to an amplitude deviation less than 5.4% from the measured
394 results. At the gauge located 2.04 m downstream of the float, the simulated wave
395 has a phase lead of about 20 degrees with respect to the measured wave. However,
396 the amplitude deviation of RANS simulation and the phase lead reach 10.8% and 32
397 degrees respectively; these accord with the improved prediction by the SPH model.

398 The results at P4 and P5 in fig.6 show the surface elevation time series to the
399 side of the float. The measured surface elevations along the wave crest almost match
400 the undisturbed incident time series. In the RANS simulation, however, flattening
401 of waveforms and larger wave heights than the incident wave were observed, which
402 were attributed to wave scattering from the float. Compared with the physical water
403 tunnel, the side walls of NWT in the RANS simulation are closer to the float and there
404 is no energy absorption from the waves. Instead, waves scattered from the float are
405 re-reflected between the side walls of the NWT, leading to the observed discrepancies
406 from the measurements. A NWT of the same dimensions is utilised in the SPH
407 simulation; however, wave scattering is not evident through either deformation of
408 the waveform or increase in wave height, though there is a phase lead of 26 degrees.

409 Fig.7 presents time histories of the horizontal and vertical force components on
410 the float. The experimental observations, present SPH predictions, and previous
411 RANS simulations are superimposed for comparison purposes. In the top panel of
412 fig.7, both SPH and RANS perform well in predicting the asymmetric horizontal
413 force on the fixed device, with the horizontal force increasing more slowly than it
414 decreases. However, the amplitude deviation of the horizontal force obtained by
415 the SPH method is 3.1%, which is smaller than the value of -18.6% obtained by
416 RANS. For the much larger vertical force, the standard deviation of 8.5% peak-peak
417 value between the SPH model predictions and measurements is also smaller than the
418 corresponding standard deviation of 10.3% for the RANS model. This confirms the
419 suitability of the SPH method to predict the temporal evolution of the forces on the
420 device. Besides, the improved performance of SPH is also confirmed by the smaller
421 phase lead incurred between the predicted and experimental waveforms than for the
422 RANS model.

423 In short, the SPH method provides accurate predictions of the surface elevations
424 in the vicinity of the float and the loads on the float, and reproduces a reliable picture
425 of the relatively complex flows in the case of a fixed device.

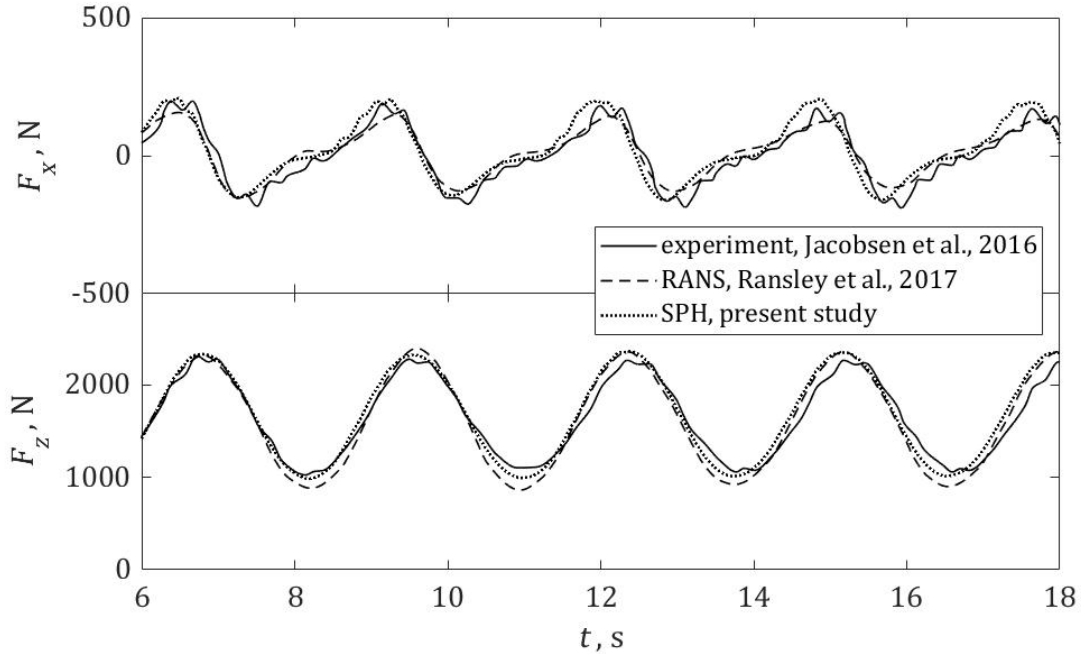


Figure 7: Time histories of horizontal and vertical force components on the float of the fixed device with $D = 1$ m, in regular waves of height $H = 0.25$ m and period $T = 2.8$ s.

426 3.2.2. Freely pitching device

427 We now simulate the same regular wave case as before, but with the scaled model
 428 able to pitch freely about the hinge point between the support structure and the arm,
 429 and with the PTO system disabled (i.e. no PTO stiffness and damping). In this case,
 430 the motion of the float is coupled to the hydrodynamic loading of the surrounding
 431 fluid. The pitching motion is transformed into a single translation of the disabled
 432 PTO cylinder within the device constraints, i.e. X_c . Positive displacement of the
 433 cylinder corresponds to lifting of the float. After about 6 s, the different initial
 434 transients of the float position in the experiment and simulations by RANS and SPH
 435 decay, and the corresponding systems reach a stable oscillatory state driven by the
 436 incident wave.

437 Fig.8 compares the measured and predicted time series of PTO cylinder displace-
 438 ment after 6 s. Compared with measured results, the RANS simulation predicts
 439 a larger displacement amplitude, while the SPH simulation predicts less amplitude
 440 deviation but with a small phase lead of about 13 degree. Similar to the previous
 441 comparison of wave crest elevations for the fixed device, the deviations of SPH and
 442 RANS-VoF simulations from measurements on the freely pitching device are due to

443 re-reflection of scattered/radiated waves from the float by side walls of the narrow
 444 NWT and consequent interference with incident waves at the float location.

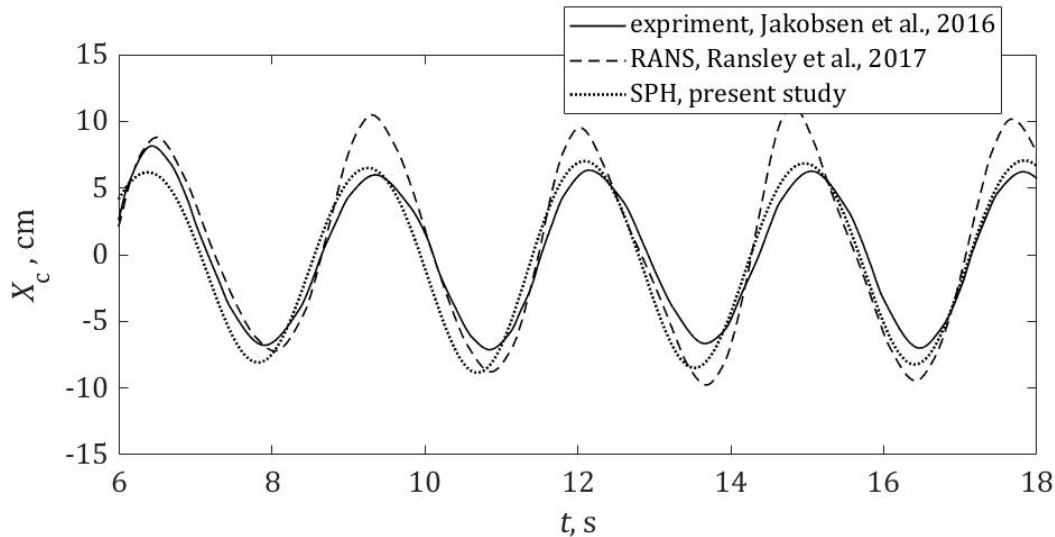


Figure 8: PTO cylinder displacement time history of the freely pitching device with $D = 1$ m in regular waves of height $H = 0.25$ m and period $T = 2.8$ s.

445 Fig.9 compares time series of horizontal and vertical forces obtained from the
 446 SPH simulation with the available experimental results by Jakobsen et al. [24] from
 447 $t = 20$ to 27 s. This duration is enough to validate the SPH model, because the
 448 force components have evolved into a steady state and shown the similarity between
 449 wave cycles. The numerical model provides a satisfactory prediction of the temporal
 450 evolution of the force components, including their asymmetry. The standard deviation
 451 between simulated and experimental values of the overall force over 7 s is 7.6%
 452 peak-peak value of the varied force. The amplitude deviation of the horizontal force
 453 is -5.7% and the phase lead of the vertical force is approximately zero.

454 3.2.3. Extreme waves

455 The foregoing two cases of fixed and freely pitching device by the SPH modelling,
 456 with $D = 1$ m, subject to regular waves of height $H = 0.25$ m and period $T = 2.8$ s,
 457 have demonstrated that the SPH model gives an accurate hydrodynamic representa-
 458 tion of wave height, wave phase, force components, and the device motion. In order
 459 to test the robustness of the SPH model, a steep regular wave with $H = 0.68$ m and
 460 $T = 2.0$ s is simulated with the device still able to move freely. Although Jakobsen
 461 et al. [24] did not perform tests for freely pitching device in extreme waves to avoid

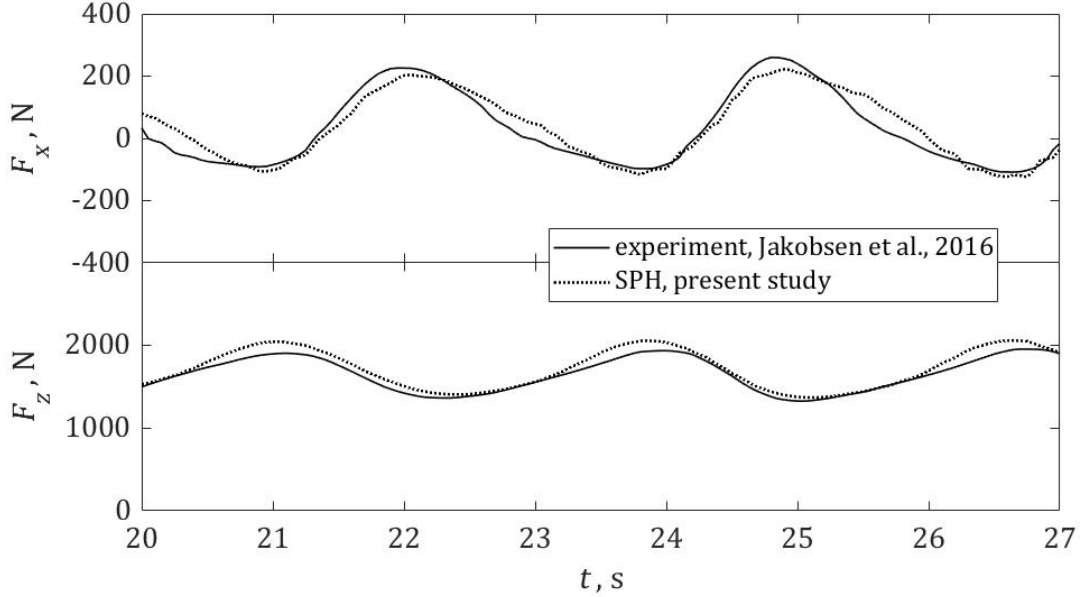


Figure 9: Horizontal (in wave propagation direction) and vertical force components on the float of a freely pitching device with $D = 1$ m subject to regular waves of height $H = 0.25$ m and period $T = 2.8$ s.

462 possible damage to the device due to excessive motion, Ransley et al. [31] provided
 463 RANS-VoF snapshots showing device-wave interaction in this case. We also report
 464 a series of SPH snapshots for the three cases with $D = 1$ m.

465 Fig.10 and fig.11 respectively illustrate the snapshots of device-wave interaction
 466 for the fixed and freely pitching device model in small-steepness waves at 4 instants
 467 during a wave cycle. The deformation of free surface neighbouring the float becomes
 468 stronger when the wave crest passes by the float, and radiated waves are very weak
 469 in these two cases.

470 Fig.12 illustrates the snapshots for the freely pitching device model in large-
 471 steepness waves. During a wave cycle the float goes from being nearly completely
 472 submerged to leaving the water altogether. Free surface deformation and radiated
 473 waves are stronger in the case of extreme waves than those in the case of small-
 474 steepness waves. The phenomenon of green water is observed when the float is
 475 pitching from the trough elevation to the peak elevation, and the phenomenon of
 476 slamming is observed when the float is pitching from the peak elevation to the trough
 477 elevation. In addition, spray is observed upstream the float at the peak elevation.
 478 These complex phenomena are handled by the present SPH simulation without issue,

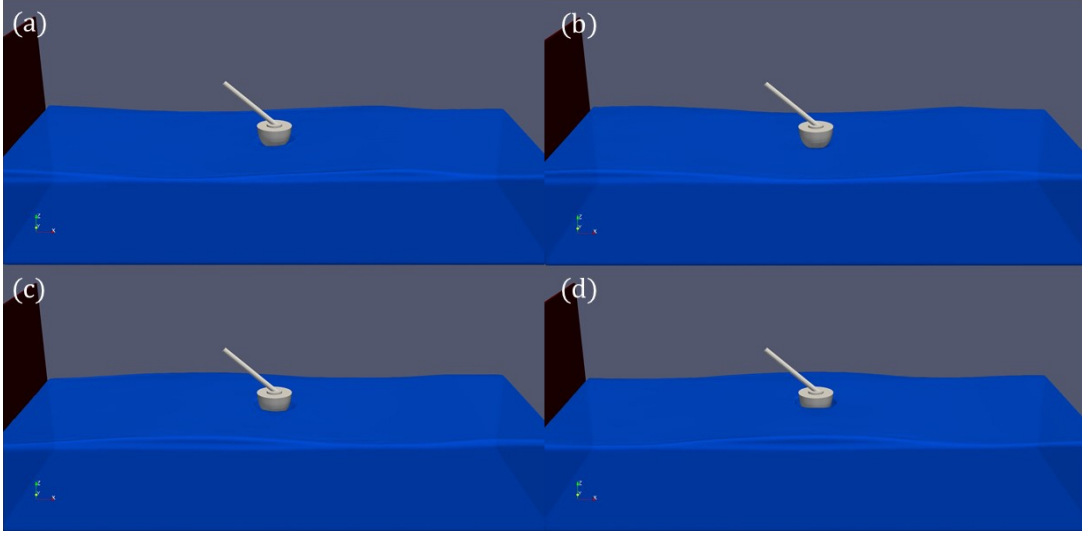


Figure 10: Snapshots of the fixed device with $D = 1$ m subject to small-steepness waves of height $H = 0.25$ m and period $T = 2.8$ s. (a) and (c) the mid wave elevations close to the float, (b) and (d) the maximum and minimum wave elevations.

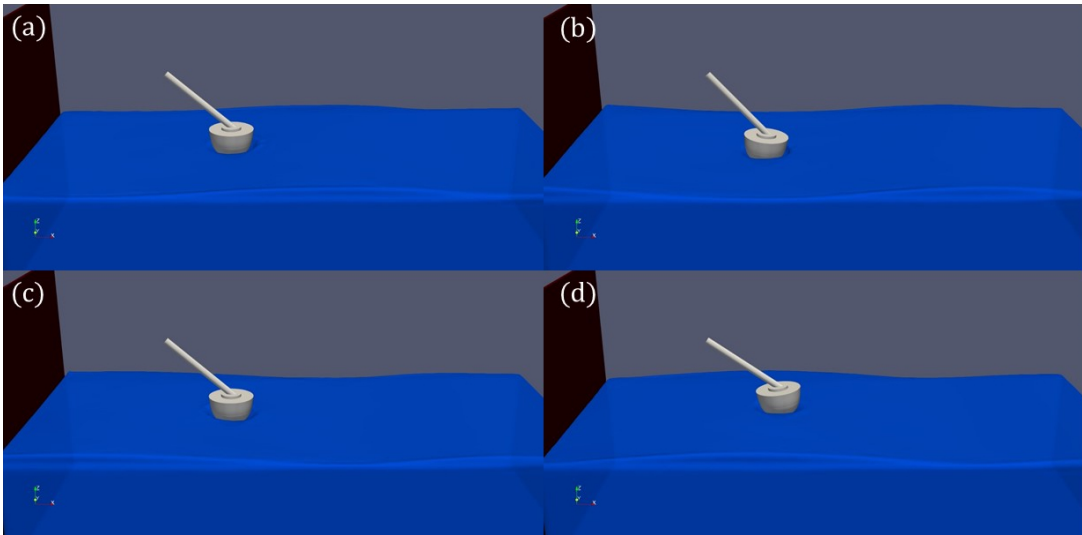


Figure 11: Snapshots of the freely pitching device with $D = 1$ m subject to small-steepness waves of height $H = 0.25$ m and period $T = 2.8$ s. (a) and (c) the mid float elevations, (b) and (d) the maximum and minimum float elevations.

479 meaning the robustness of the SPH model. The resulting observations are consistent
 480 with the numerical results by Ransley et al. [31], which further provides confidence

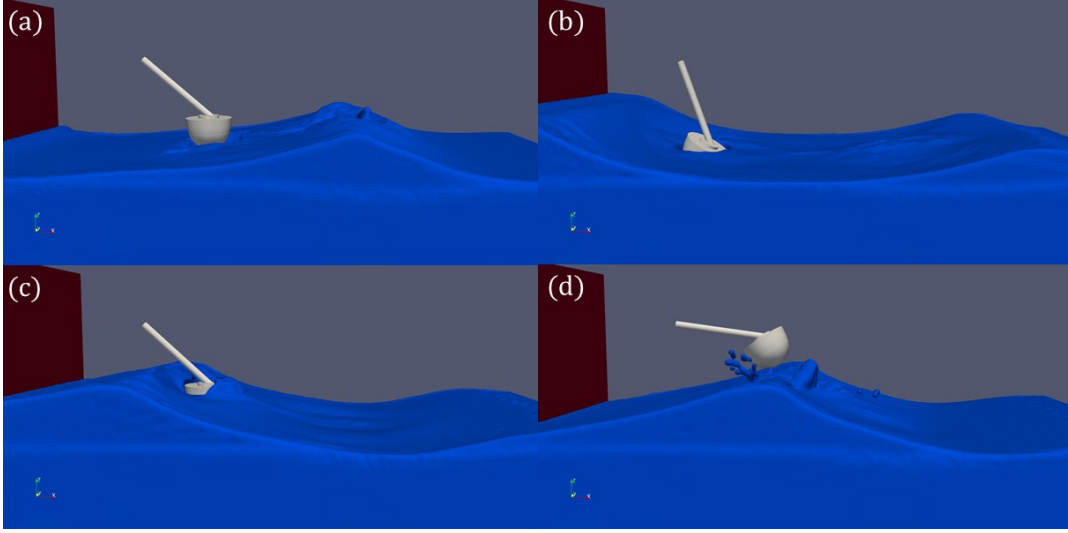


Figure 12: Snapshots of the freely pitching device with $D = 1$ m subject to large-steepness waves of height $H = 0.68$ m and period $T = 2.0$ s. (a) and (c) the mid float elevations, (b) and (d) the maximum and minimum float elevations.

481 in predicting the power conversion performance of a top-mounted pitching point
 482 absorber.

483 4. Predicted power conversion performance of devices at different scales

484 A parameter study is next undertaken for the power conversion performance
 485 of the top mounted pitching point absorber with the PTO system engaged. The
 486 NWT and device are simulated at different scales using a similar numerical setup as
 487 above (see fig.5 and table 2). We assume that the configuration of the small-scale
 488 NWT and device in Section 3.1 is valid across different scales and with the PTO
 489 engaged [67, 68]. The influence of wave conditions (wave height and period) on
 490 power conversion performance and on the PTO damping coefficient are considered.

491 The PTO is modelled as a spring-damping system that links the support structure
 492 and the arm of the pitching device as shown in fig.2, with zero stiffness and adjustable
 493 damping, governed by Newton's second law:

$$M \frac{d\vec{v}_r}{dt} = \vec{F}_e + \vec{F}_d, \quad (6)$$

494 where M and \vec{v}_r are the mass and relative velocity of the PTO, \vec{F}_d is the damping
 495 force, and \vec{F}_e is the excitation force exerted by the pitching point absorber. The

496 linear damping is adopted, i.e. the damping force is written as

$$\vec{F}_d = -C\vec{v}_r, \quad (7)$$

497 where C is the damping coefficient. Note that C approaches infinity for a fixed
 498 pitching device, whereas C is zero for a freely pitching device. PTO damping is the
 499 mechanical force that extracts power from the wave-induced motion of a pitching
 500 float. In order to improve the energy conversion efficiency, the PTO system is de-
 501 signed to run in slow relative motion with limited mass such that the inertial force is
 502 negligible compared to the damping force. Accordingly, the power absorbed by the
 503 device can be estimated by the PTO damping as follows:

$$P = \frac{1}{3T} \sum_{n=1}^{3T/\Delta t} C\vec{v}_{rn} \cdot \vec{v}_{rn}\Delta t = \frac{1}{3T} \sum_{n=1}^{3T/\Delta t} C|\vec{v}_{rn}|^2\Delta t, \quad (8)$$

504 where P is the absorbed power, T is the wave period, Δt is the time step specified
 505 as 0.05 s, and \vec{v}_{rn} is the relative velocity vector at time step n . The total summing
 506 time is specified as the last three steady wave periods. Note that energy losses in
 507 the power conversion system and in the transmission system are neglected, i.e. 100%
 508 PTO efficiency is adopted. In addition to the converted power P , the quantity CWR
 509 [16] is introduced here to quantify the performance of the device according to its
 510 scale dimension and the incident wave conditions:

$$\text{CWR} = \frac{P}{DP_w}, \quad (9)$$

511 where D is the referential diameter of the device and $P_w = \rho g^2 H^2 T / 32\pi$ is the
 512 incident power in regular waves of wave height H and period T . ρ is water density,
 513 and g is the acceleration due to gravity.

514 4.1. Device with $D = 1$ m

515 This section examines wave energy conversion by a device with $D = 1$ m in
 516 regular incident waves. Fig.13 shows the time series of the magnitude of the relative
 517 velocity vector $|\vec{v}_r|$ in the top panel and the PTO absorbed power P in the bottom
 518 panel for varying damping coefficients in the range of $0 \leq C \leq 8 \times 10^4$ Ns/m with
 519 $H = 0.25$ m and $T = 2.8$ s. The amplitude of $|\vec{v}_r(t)|$ is observed to decrease with
 520 increasing C . Compared to the kinematics of the freely pitching device, a time delay
 521 occurs for the damped device with the PTO enabled, and the time delay is observed
 522 to increase along with C . Different from the above-mentioned monotonous changes
 523 caused by the PTO damping, P first increases rapidly and then gradually decreases

524 with increasing C . The peak power over the damping coefficient range is located at
 525 $C = 2.0 \times 10^4$ Ns/m, exhibiting a uni-modal distribution of P in terms of C . This
 526 uni-modal distribution means the short-term optimal operation of the device with a
 527 certain wave period can be achieved by adjusting the PTO damping. Accordingly,
 528 three damping coefficients respectively smaller than, equal to and larger than the
 529 damping coefficient absorbing the most power are studied for each scaled device to
 530 give insights into the effects of T and H on the wave conversion performance.

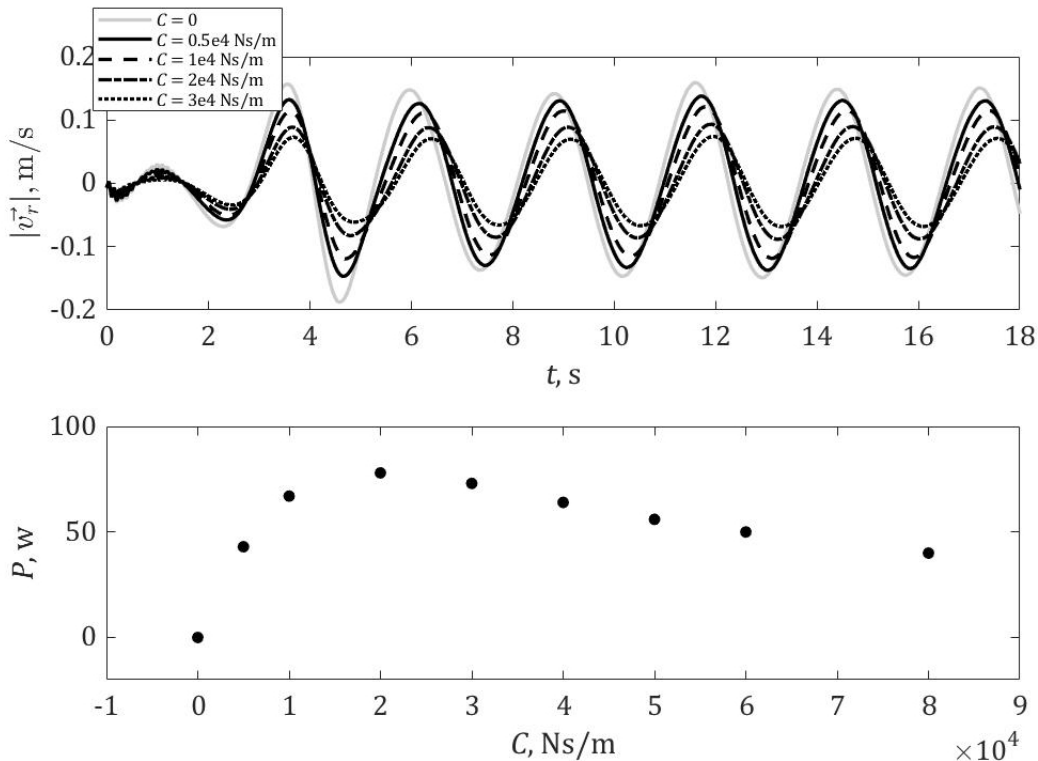


Figure 13: Top: time series of $|\vec{v}(t)|$ for $C = 0, 0.5, 1.0, 2.0,$ and 3.0×10^4 Ns/m (gray solid, black solid, dashed, dash-dotted, dotted lines); bottom: P versus C . $D = 1$ m, $H = 0.25$ m and $T = 2.8$ s.

531 Fig.14 presents the standard deviation value of damping force $\sigma(F_d)$, the PTO
 532 absorbed power P , and the capture width ratio CWR with varying wave period T
 533 for wave heights $H = 0.25$ and 2.0 m and damping coefficients $C = 1.0, 2.0,$ and
 534 6.0×10^4 Ns/m. In all cases reported in fig.14, $\sigma(F_d)$ and P have the same trend,
 535 i.e. they increase first and then decrease with increasing T . The reason for the same
 536 trend is that in the case of ideal PTO, damping forces balance PTO excitation forces
 537 exerted by the float and directly do work to produce the output power with the

538 intrinsic relation of $\sigma(F_d) = \sqrt{CP}$. Only one peak occurs over the period range of
 539 simulated waves, exhibiting a uni-modal distribution of $\sigma(F_d)$ and P in terms of T .
 540 The wave periods at which the peaks of $\sigma(F_d)$ and P occur are the same, and are
 541 found to increase with PTO damping.

542 The uni-modal behaviours of P with C and T implies that a one-to-one corre-
 543 spondence of C and T exists for the peak P . This is meaningful for the targeted
 544 operation of the PTO system to achieve the short-term optimal energy conversion
 545 performance with varying wave period. Specifically, the PTO damping coefficient
 546 should be adjusted to a corresponding larger value for an increased wave period,
 547 and to a certain smaller value for a decreased wave period. A PTO with a damping
 548 coefficient of $C = 2.0 \times 10^4$ Ns/m absorbs more energy from waves of period in the
 549 range of $1 < T < 5$ s than PTOs with other damping coefficients, which is proved to
 550 be the global optimal PTO damping for the device with $D = 1$ m. Furthermore, the
 551 peak absorbed power with the optimal damping is found to be the largest one among
 552 those power peaks with different damping coefficients. For $C = 2.0 \times 10^4$ Ns/m, the
 553 power peak occurs at wave period $T = 2.8$ s. This optimal wave period (2.8 s) is
 554 noted to be larger than the natural period (1.9 s) of the freely pitching device.

555 Although more power is captured from waves of $H = 2.0$ m by a PTO with fixed
 556 C , the normalised quantity CWR is larger for $H = 0.25$ m. In addition, the wave
 557 period corresponding to the CWR peak is no larger than that corresponding to the
 558 power peak for different H and C . The different behaviours of P and CWR with
 559 H and T can be explained by dimensional analysis. According to the definition of
 560 CWR, the effect of H and T on CWR is written as $CWR(H, T) \sim P(H, T)/TH^2$.
 561 For the same T and C , the ratio of P with $H = 2.0$ m over P with $H = 0.25$ m
 562 is basically a constant of 24.0, leading to a constant shift between P curves with
 563 different H and the same C in the middle panel of fig.14. Hence, the ratio of CWR
 564 with $H = 2.0$ m over CWR with $H = 0.25$ m is 0.375 for fixed T and C . Also
 565 because $CWR(T) \sim P(T)/T$, the peak CWR moves at smaller T compared to the
 566 peak P for fixed C and H .

567 As wave steepness progressively increases with larger wave height for a fixed
 568 wave period, or with smaller wave period for a fixed wave height, nonlinear interac-
 569 tion between the device and waves increasingly strengthens under the influence of
 570 slamming and green water processes. For the device with enabled PTO, the PTO
 571 damping also affects the occurrence of these complex phenomena. Compared with
 572 the freely pitching device, the pitching movement of the float is damped when the
 573 PTO system is absorbing the wave energy. Hence, the green water become stronger
 574 while the slamming become weaker with increased PTO damping. Despite the hy-
 575 drodynamic complexity at large wave steepness and varying PTO damping, the SPH

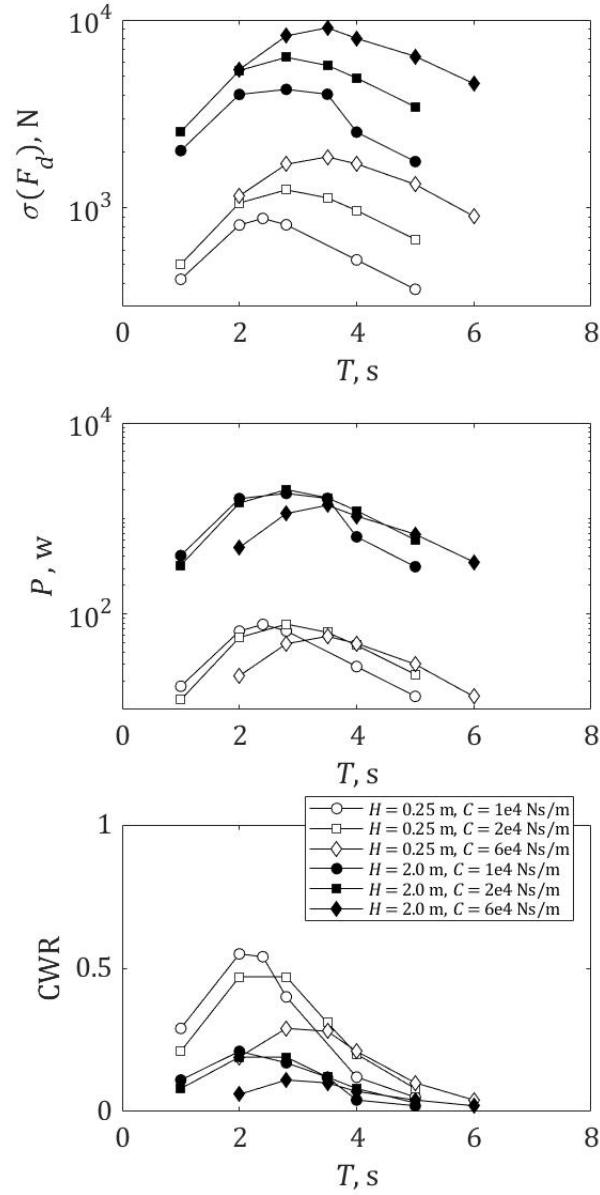


Figure 14: Wave energy conversion performance (upper plot: $\sigma(F_d)$; middle plot: P ; lower plot: CWR) as a function of T for $H = 0.25$ and 2.0 m (open, closed symbols) and $C = 1.0, 2.0,$ and 6.0×10^4 Ns/m (circle, square and diamond symbols). $D = 1$ m.

576 model nevertheless remains reliable and stable.

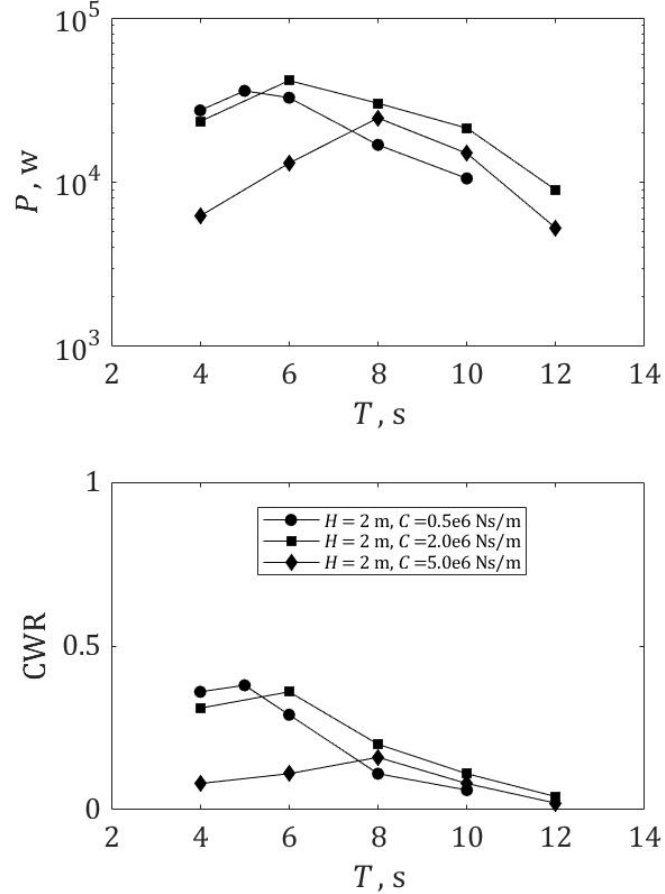


Figure 15: Wave energy conversion performance (upper plot: P ; lower plot: CWR) as a function of T for $H = 2.0$ m and $C = 0.5, 2.0,$ and 5.0×10^6 Ns/m (circle, square and diamond symbols). $D = 5$ m.

578 We next consider a device with $D = 5$ m subject to waves with the constant height
 579 of $H = 2$ m. The natural period of the device is 4.2 s. At the initial moment, the
 580 water-plane diameter of this scaled device is 4.9 m and the draught is 2.0 m. Fig.15
 581 displays the influence of PTO damping coefficient on the wave energy conversion
 582 performance curves. The reported damping coefficients $C = 0.5, 2.0,$ and $5.0 \times$
 583 10^6 Ns/m are chosen according to the same criterion as in the case of $D = 1$ m,
 584 and the uni-modal distribution of absorbed power with wave period is observed

585 for different damping coefficients. The power converted by a single point absorber
586 with $D = 5$ m reaches a maximum of 42 kW when the PTO damping coefficient is
587 2.0×10^6 Ns/m. Although the damping coefficient of $C = 0.5 \times 10^6$ Ns/m is better
588 for $4 \leq T \leq 5$ s, $C = 2.0 \times 10^6$ Ns/m gives the best performance in the wider
589 wave period range of $4 \leq T \leq 12$ s. The same trend of P with T applies to the
590 CWR curves. It is noted that the CWR peak with the optimal damping is not the
591 maximum among those with different C for $D = 5$ m. The inconsistent behaviours
592 of P and CWR are attributed to the coupled effects of T and C according to the
593 relation of $\text{CWR}(T, C) \sim P(T, C)/T$ as drawn for $D = 1$ m.

594 4.3. Device with $D = 1 \sim 10$ m

595 To examine scale effect on energy conversion performance, simulations are carried
596 out for devices with D ranging from 1 to 10 m in regular incident waves of height
597 $H = 2$ m. For the device with $D = 10$ m, the natural period is 6.0 s and the initial
598 draught and water-plane diameter are respectively 4.0 m and 9.8 m. We also observe
599 the uni-modal distribution of absorbed power versus wave period for $D = 10$ m as
600 in the cases of $D = 1, 5$ m. By searching for the highest one among the peaks of
601 the uni-modal distributions with different C , we achieve the optimal damping for
602 each scaled device. All these devices operate under optimal damping of absorbed
603 power; in other words $C_o = 2 \times 10^4$ Ns/m for $D = 1$ m, $C_o = 2 \times 10^6$ Ns/m for
604 $D = 5$ m and $C_o = 5 \times 10^7$ Ns/m for $D = 10$ m, where the subscript o indicates
605 optimal. The upper panel of fig.16 shows the uni-modal distribution of P with T
606 for $D = 1 \sim 10$ m. Both the absorbed power and the wave period pertaining to the
607 peak of the uni-modal distribution increase with the increasing device scale. The
608 results indicate that a device with $D = 10$ m generates about 10 times more power
609 than a device with $D = 5$ m and 300 times more than a device with $D = 1$ m. As
610 D increases from 1 to 10 m, CWR increases from 0.2 to about 1.0, implying that
611 the larger device, when optimally damped, can absorb energy from longer incident
612 waves with fixed wave height.

613 5. Discussion of optimal power

614 5.1. Scale effect

615 An understanding of scale effect on optimal absorbed power is important in device
616 design. Here, optimal power P_o and associated wave period T_o are identified from the
617 power curves of devices with different float diameters D and corresponding optimal
618 damping coefficients C_o (see fig.16). The upper plot in fig.17 shows the behaviour of
619 P_o , T_o and C_o with varying D . Linear fits have been made to the simulated results in

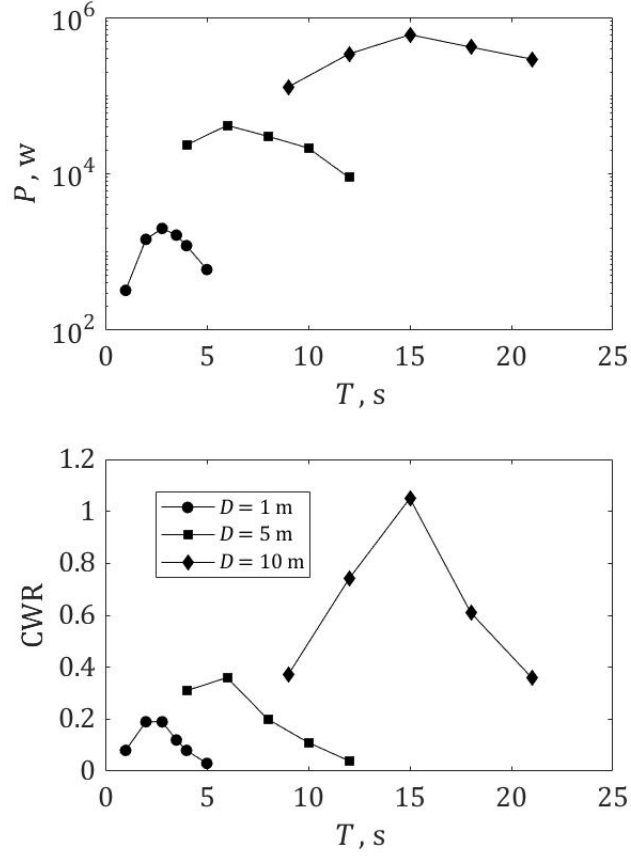


Figure 16: Wave energy conversion performance (upper plot: P ; lower plot: CWR) as a function of wave period T under optimised PTO damping conditions for $D = 1, 5,$ and 10 m indicated by circle, square and diamond symbols.

620 the log-log plot, and the following empirical relationships obtained from the limited
 621 data:

$$\begin{aligned}
 P_o &\propto 1.58 \times 10^3 \cdot D^{2.4}, \\
 T_o &\propto 2.51 \cdot D^{0.7}, \\
 C_o &\propto 1.58 \times 10^4 \cdot D^{3.3}.
 \end{aligned}
 \tag{10}$$

622 The above empirical relations are limited to regular incident wave conditions of con-
 623 stant height and period, and to a PTO system with zero-stiffness, linear damping,
 624 and 100% efficiency. These are obvious simplifications compared to actual field de-
 625 ployment situations. Even so, the scaling relations inherently include hydrodynamic

626 Froude number Fr and Reynolds number Re effects and the dynamic effect of the
 627 PTO itself. For the freely pitching device, the Fr scaling law is dominant and the
 628 Re scaling law is of very minor importance under typical operating wave conditions.
 629 However, for the device with enabled PTO, the hydrodynamics of the float and the
 630 dynamics of the PTO are coupled together to form a more complicated system. In
 631 addition to $Fr&Re$ effects, the effect of PTO damping should be considered.

632 Through dimensional analysis, the absorbed power, the wave period, and the
 633 PTO damping are respectively proportional to $D^{3.5}$, $D^{0.5}$ and D^2 solely according
 634 to the Fr scaling law, while are proportional to D^2 , D^2 and D^5 solely according
 635 to the Re scaling law. The observed scaling behaviours of the optimal absorbed
 636 power ($P_o \sim D^{2.4}$), wave period ($T_o \sim D^{0.7}$), and damping coefficient ($T_o \sim D^{3.3}$)
 637 deviate from the Fr scaling law which dominates the hydrodynamics of the freely
 638 pitching device. These deviations should be due to the coupled effect of the PTO
 639 damping. However, neither well-defined dimensionless quantity (e.g. damping ratio
 640 in a spring-damping-oscillator system) nor corresponding scaling law (similar to the
 641 hydrodynamic $Fr&Re$ laws) is available to characterise the damping effect in the
 642 PTO system with zero-stiffness. Hence, further quantitative studies on the device
 643 performance with enabled PTO are needed to resolve the combined scaling effects.

644 5.2. Effect of water depth

645 Among physical conditions at the deployment site of a WEC, the water depth
 646 is a basic one relevant for wave energy conversion. The effect of water depth h on
 647 energy conversion with optimal PTO damping is now discussed briefly. According
 648 to the linear potential theory for unconstrained axisymmetrical point absorbers [69],
 649 the upper limit of absorbed power by an optimally controlled float is $P_w \lambda_I / 2\pi$, where
 650 λ_I is the regular wave length as $h \rightarrow \infty$. This power limit is independent of float
 651 diameter. Then, the theoretical CWR at the upper power limit is

$$\text{CWR}_{th} = \frac{P_w \lambda_I / 2\pi}{P_w D} = \frac{gT^2}{4\pi^2 D}. \quad (11)$$

652 Note that CWR_{th} is essentially the limit efficiency of a point absorber deployed in
 653 the deep water.

654 The lower plot of fig.17 shows the relationship between $\text{CWR}/\text{CWR}_{th}$ and $h \times$
 655 $2\pi/\lambda$ (where λ is the wavelength in water of finite depth h), which indicates the in-
 656 fluence of dimensionless water depth on energy conversion efficiency with the optimal
 657 PTO damping. For $D = 1, 5$ m, $\text{CWR}/\text{CWR}_{th}$ monotonically increases along with
 658 $2\pi h/\lambda$ in the range of $0.7 < 2\pi h/\lambda < 12$. Waves travelling from deep water to shal-
 659 low water suffer increasingly from bottom friction, making less available wave energy.

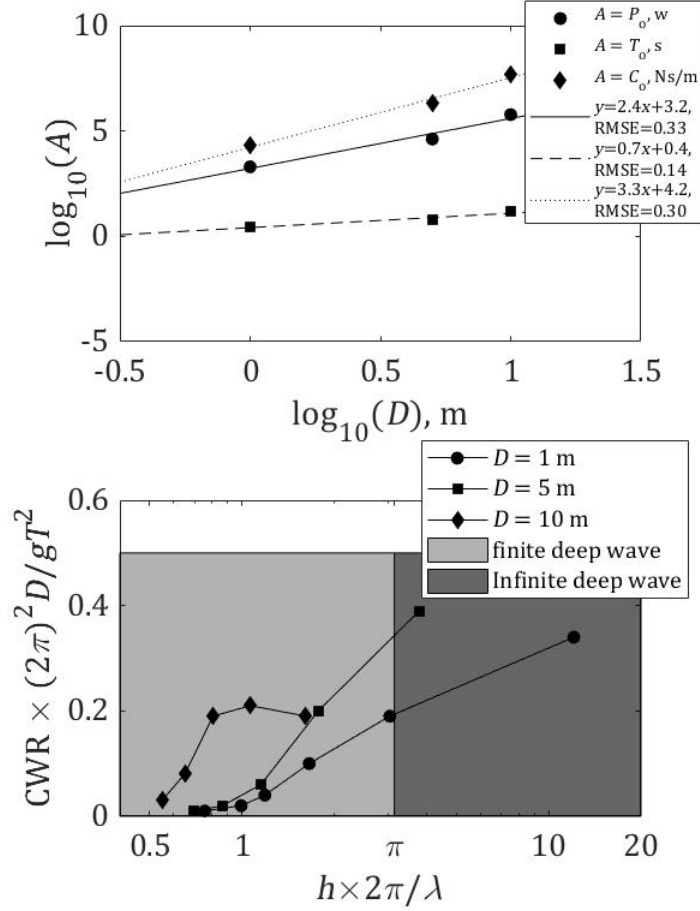


Figure 17: Upper plot: log-log optimal P_o (circle), T_o (square) and C_o (diamond) as functions of D . Corresponding linear fits are presented as solid, dashed, and dotted lines. Lower plot: CWR/CWR_{th} as a function of $h \times 2\pi/\lambda$ for $D = 1, 5, 10$ m (circle, square and diamond symbols) in water depth that is infinite (dark) and finite (light).

660 Assumed that a device with a fixed PTO damping has a fixed energy conversion abil-
661 ity, the wave energy conversion efficiency CWR gradually increases to its limit value
662 CWR_{th} with increasing water depth. However, for $D = 10$ m, a local optimal water
663 depth seems to exist close to $2\pi h/\lambda = 1.1$. This trend with dimensionless water
664 depth in the finite deep water is consistent with the linear inviscid modelling of a
665 heaving buoy by Garnaud & Mei [70, 71], but the viscous effect leads to relatively low
666 efficiency in the present SPH modelling. It is worthy of further study whether an in-

667 creasing trend of CWR/CWR_{th} with $2\pi h/\lambda$ can be achieved in the infinite deep water
668 for the larger device. In addition, it is noted that the larger device always converts
669 wave energy with higher efficiency in the range of $0.5 < 2\pi h/\lambda < 1.6$ compared with
670 the smaller ones. In deep water ($2\pi h/\lambda > \pi$), waves travel almost without energy loss
671 across the ocean, and predictions of device performance by testing and modelling are
672 easy to transfer for siting. However, devices in shallow water ($2\pi h/\lambda < \pi/10$) have
673 different structural solutions and facilitated access to grid connection and equipment
674 maintenance with low costs. Taking into consideration a trade-off of available energy
675 and costs, the most appropriate site for a top-mounted pitching point absorber is
676 usually in finite deep water ($\pi/10 < 2\pi h/\lambda < \pi$). Hence, the peak efficiency of the
677 larger device at water depth of $2\pi h/\lambda = 1.1$ provides reference for device siting.

678 6. Conclusions

679 Owing to its inherent advantages in capturing rapidly deforming free surface
680 flows, a meshless SPH model was used to investigate the power conversion perfor-
681 mance of a top-mounted pitching point absorber. The SPH model gave free surface
682 motions in satisfactory agreement with experimental measurements of wedge entry
683 into otherwise still water, properly representing extreme free surface motion events
684 during the wedge immersion stages, including slamming, green water, splash, break-
685 up, and recombination. For a geometrically complex wave energy conversion device
686 such as Wavestar, accurate modelling of the interaction between water free surface
687 and device is key to solving the overall fluid-structure problem, which is important
688 in survivability and performance assessments.

689 The SPH simulations show good agreement with the measurements and the
690 RANS-VoF predictions of characteristic hydrodynamic behaviours of fixed and freely
691 pitching devices fitted with an 1 m diameter absorber subject to the same incident
692 wave conditions. Only limited phase leads were found in the SPH simulations of
693 the surface elevation beside the fixed model and the PTO displacement of the freely
694 pitching model. In the case of extreme waves, the SPH modelling demonstrates
695 the robustness and handles the complex phenomena such as green water, spray and
696 slamming without issue. Execution times of the SPH simulations were not increased
697 significantly despite the wave-float-coupled kinematics and the large wave steepness.
698 The satisfactory prediction accuracy and limited computational costs of the SPH sim-
699 ulations provide confidence in further studying the power conversion performance of
700 the top-mounted pitching point absorber.

701 A study of wave energy conversion performance under different wave conditions
702 and PTO damping coefficients revealed that: absorbed power P invariably had a

703 uni-modal distribution with damping coefficient C and wave period T over the range
704 of test cases considered; the wave period corresponding to peak absorbed power
705 increased with the PTO damping. The uni-modal behaviours of P with C and T
706 is meaningful for the targeted operation of the PTO system to achieve the short-
707 term optimal energy conversion performance with varying wave period. In addition,
708 inconsistent behaviours of absorbed power P and capture width ratio CWR with
709 varied wave height H were observed, which can be explained according to the relation
710 $CWR(H, T, C) \sim P(H, T, C)/TH^2$.

711 A further study examined the effects of scale and water depth on energy con-
712 version with optimal PTO damping. It was found that a device with $D = 10$ m
713 generated about 300 times more power than one with $D = 1$ m. As D increased
714 from 1 m to 10 m, CWR increased from 0.2 to about 1.0, implying that a larger
715 device that is optimally damped is increasingly effective at absorbing energy from
716 long incident waves of maximum wave height. Optimal absorbed power, wave period
717 and PTO damping exhibited a power law relationship with device scale. Because of
718 the combined Fr & Re effects and the PTO damping effect, scaling behaviours of the
719 optimally damped pitching device deviate from the Fr scaling law which dominates
720 the hydrodynamics of the freely pitching device. In terms of water depth, a small
721 device ($D = 1, 5$ m) appears higher efficiency of extracting energy from deep water
722 waves than from shallower water waves, whereas a large device ($D = 10$ m) achieves
723 the maximum efficiency in water of finite depth provided $0.5 < 2\pi h/\lambda < 1.6$. In
724 the water of finite depth, the larger device always converts wave energy with higher
725 efficiency compared with the smaller ones. The peak efficiency of the larger device
726 at water depth of $2\pi h/\lambda = 1.1$ provides reference for device siting.

727 Acknowledgements

728 This work was supported by the National Key Research and Development Plan
729 of China (Nos. 2019YFB1504402, 2017YFE0132000 and 2018YFB1501202), the Na-
730 tional Natural Science Foundation of China (No. 11872248) and the Self-directed
731 Research Subject of the State Key Laboratory of Marine Engineering, Shanghai Jiao
732 Tong University (No. GKZD010075). The authors would like to thank Hongliang
733 Wang and Jianguo Gong for their assistance in the experiments.

734 References

- 735 [1] C. V. C. Weiss, R. Guanche, B. Ondiviela, O. F. Castellanos, J. Juanes, Ma-
736 rine renewable energy potential a global perspective for offshore wind and wave
737 exploitation, *Energy Convers. Manage.* 177 (2018) 43–54.

- 738 [2] A. F. d. O. Falcão, Wave energy utilization: a review of the technologies, *Renew.*
739 *Sustain. Energy Rev.* 14 (2010) 899–918.
- 740 [3] Wave Dragon, Prototype testing in Denmark, [http://www.wavedragon.net/](http://www.wavedragon.net/prototype-testing-in-denmark)
741 [prototype-testing-in-denmark](http://www.wavedragon.net/prototype-testing-in-denmark) (2009).
- 742 [4] S. Oliveira-Pinto, F. Taveira-Pinto, T. Morais, P. Rosa-Santos, Experimental
743 evaluation of the effect of wave focusing walls on the performance of the sea-
744 wave slot-cone generator, *Energy Convers. Manage.* 110 (2016) 165–175.
- 745 [5] A. Al-Habaibeh, D. Su, J. McCague, A. Knight, An innovative approach for
746 energy generation from waves, *Energy Convers. Manage.* 51 (2010) 1664–1668.
- 747 [6] Ocean Power Technologies, PB3 POWERBUOY, [https://](https://oceanpowertechnologies.com/pb3-powerbuoy)
748 oceanpowertechnologies.com/pb3-powerbuoy (2011).
- 749 [7] R. Curran, T. J. T. Whittaker, T. P. Stewart, Aerodynamic conversion of ocean
750 power from wave to wire, *Energy Convers. Manage.* 39 (1998) 1919–1929.
- 751 [8] Tethys, OES-Environmental Metadata - Oceanlinx MK3, [https://tethys.](https://tethys.pnnl.gov/project-sites/oceanlinx-mk3)
752 [pnnl.gov/project-sites/oceanlinx-mk3](https://tethys.pnnl.gov/project-sites/oceanlinx-mk3) (2016).
- 753 [9] Energy Island, Lilypad - Wave Energy Conversion, [http://www.energyisland.](http://www.energyisland.com/projects/lilypad/lilypad.html)
754 [com/projects/lilypad/lilypad.html](http://www.energyisland.com/projects/lilypad/lilypad.html) (2009).
- 755 [10] Y. Li, Y. H. Yu, A synthesis of numerical methods for modeling wave energy
756 converter-point absorbers, *Renew. Sust. Energ. Rev.* 16 (2012) 4352–4364.
- 757 [11] Y. Liu, Y. Li, F. He, H. Wang, Comparison study of tidal stream and wave
758 energy technology development between China and some Western Countries,
759 *Renew. Sustain. Energy Rev.* 76 (2017) 701–716.
- 760 [12] World Energy Council, World Energy Perspective, Cost of Energy Tech-
761 nologies, [https://www.worldenergy.org/assets/downloads/WEC_J1143_](https://www.worldenergy.org/assets/downloads/WEC_J1143_CostofTECHNOLOGIES_021013_WEB_Final.pdf)
762 [CostofTECHNOLOGIES_021013_WEB_Final.pdf](https://www.worldenergy.org/assets/downloads/WEC_J1143_CostofTECHNOLOGIES_021013_WEB_Final.pdf) (2013).
- 763 [13] Y. Li, B. J. Lence, S. M. Calisal, An integrated model for estimating energy cost
764 of a tidal current turbine farm, *Energy Convers. Manage.* 52 (2011) 1677–1687.
- 765 [14] Y. Li, L. Willman, Feasibility analysis of offshore renewables penetrating local
766 energy systems in remote oceanic areas - A case study of emissions from an
767 electricity system with tidal power in Southern Alaska, *Applied Energy* 117
768 (2014) 42–53.

- 769 [15] R. Carballo, G. Iglesias, A methodology to determine the power performance of
770 wave energy converters at a particular coastal location, *Energy Convers. Man-*
771 *age*. 61 (2012) 8–18.
- 772 [16] A. Babarit, A database of capture width ratio of wave energy converters, *Renew.*
773 *Energy* 80 (2015) 610–628.
- 774 [17] A. Babarit, J. Hals, M. M. J., A. Kurniawan, T. Moan, J. Krokstad, Numerical
775 benchmarking study of a selection of wave energy converters, *Renew. Energy* 41
776 (2012) 44–63.
- 777 [18] M. M. Jakobsen, G. Iglesias, M. M. Kramer, V. E., Experimental study of
778 forces on point absorber, in: *5th International Conference on The Application*
779 *of Physical Modelling to Port and Coastal Protection, 2014*, pp. 15–24.
- 780 [19] C. Perez-Collazo, D. Greaves, G. Iglesias, Hydrodynamic response of the WEC
781 sub-system of a novel hybrid wind-wave energy converter, *Energy Convers. Man-*
782 *age*. 171 (2018) 307–325.
- 783 [20] S. Oliveira-Pinto, P. Rosa-Santos, F. Taveira-Pinto, Assessment of the potential
784 of combining wave and solar energy resources to power supply worldwide offshore
785 oil and gas platforms, *Energy Convers. Manage.* 223 (2020) 113299.
- 786 [21] B. Jiang, X. Li, S. Chen, Q. Xiong, B. Chen, R. G. Parker, L. Zuo, Performance
787 analysis and tank test validation of a hybrid ocean wave-current energy converter
788 with a single power takeoff, *Energy Convers. Manage.* 224 (2020) 113268.
- 789 [22] L. Berggren, M. Johansson, Hydrodynamic coefficients of a wave energy device
790 consisting of a buoy and a submerged plate, *Appl. Ocean Res.* 14 (1992) 51–58.
- 791 [23] M. Kramer, L. Marquis, P. Frigaard, Performance evaluation of the Wavestar
792 prototype, in: *9th European Wave and Tidal Energy Conference, 2011*, pp. 5–9.
- 793 [24] M. M. Jakobsen, S. Beatty, G. Iglesias, M. M. Kramer, Characterization of loads
794 on a hemispherical point absorber wave energy converter, *Int. J. Mar. Energy*
795 13 (2016) 1–15.
- 796 [25] M. Penalba, A. Mérigaud, J.-C. Gilloteaux, J. V. Ringwood, Influence of non-
797 linear Froude-Krylov forces on the performance of two wave energy points ab-
798 sorbers, *J. Ocean Eng. Mar. Energy* 3 (2017) 209–220.

- 799 [26] S. Jin, R. J. Patton, B. Guo, Viscosity effect on a point absorber wave en-
800 ergy converter hydrodynamics validated by simulation and experiment, *Renew.*
801 *Energy* 129 (2018) 500–512.
- 802 [27] Y. Yu, Y. Li, Preliminary results of a RANS simulation for a floating point
803 absorber wave energy system under extreme wave conditions, in: *Proceedings*
804 *of the ASME 30th International Conference on Ocean, Offshore, and Arctic*
805 *Engineering*, 2011, pp. 1–8.
- 806 [28] Q. Xu, Y. Li, Y. Yu, B. Ding, Z. Jiang, Z. Lin, B. Cazzolato, Experimental
807 and numerical investigations of a two-body floating-point absorber wave energy
808 converter in regular waves, *J. Fluid Struct.* 91 (2019) 102613.
- 809 [29] O. M. Faltinsen, M. Greco, M. Landrini, Green water loading on a FPSO, *J.*
810 *Offshore Mech. Arct. Eng.* 124 (2002) 97–103.
- 811 [30] Y.-H. Yu, Y. Li, Reynolds-Averaged Navier–Stokes simulation of the heave per-
812 formance of a two-body floating-point absorber wave energy system, *Comput.*
813 *Fluids* 73 (2013) 104–114.
- 814 [31] E. J. Ransley, D. M. Greaves, A. Raby, D. Simmonds, M. M. Jakobsen,
815 M. Kramer, RANS-VOF modelling of the Wavestar point absorber, *Renew.*
816 *Energy* 109 (2017) 49–65.
- 817 [32] Q. Hu, Y. Li, Unsteady RANS simulations of Wells turbine under transient flow
818 conditions, *J. Offshore Mech. Arct.* 140 (2018) 011901.
- 819 [33] H. Chen, L. Qian, Z. Ma, W. Bai, Y. Li, D. Causon, C. Mingham, Application
820 of an overset mesh based numerical wave tank for modelling realistic free-surface
821 hydrodynamic problems, *Ocean Engineering* 176 (2019) 97–117.
- 822 [34] R. A. Gingold, J. J. Monaghan, Smoothed particle hydrodynamics: theory and
823 application to non-spherical stars, *Mon. Not. R. Astr. Soc.* 181 (1977) 375–389.
- 824 [35] L. B. Lucy, A numerical approach to the testing of the fission hypothesis, *Astron.*
825 *J.* 82 (1977) 1013.
- 826 [36] A. Zhang, P. Sun, F. Ming, An SPH modeling of bubble rising and coalescing
827 in three dimensions, *Comput. Methods Appl. Mech. Eng.* 294 (2015) 189–209.
- 828 [37] C. Altomare, J. M. Domínguez, A. J. C. Crespo, J. González-Cao, T. Suzuki,
829 M. Gómez-Gesteira, P. Troch, Long-crested wave generation and absorption for
830 SPH-based DualSPHysics model, *Coast. Eng.* 127 (2017) 37–54.

- 831 [38] C. Antoci, M. Gallati, S. Sibilla, Numerical simulation of fluid-structure inter-
832 action by SPH, *Comput. Struct.* 85 (2007) 879–890.
- 833 [39] G. Oger, M. Doring, B. Alessandrini, O. Ferrant, Two-dimensional SPH simu-
834 lations of wedge water entries, *J. Comput. Phys.* 213 (2006) 803–822.
- 835 [40] K. Gong, H. Liu, B.-L. Wang, Water entry of a wedge based on SPH model with
836 an improved boundary treatment, *J. Hydrodyn.* 21 (2009) 750–757.
- 837 [41] S. Shao, Incompressible SPH simulation of water entry of a free-falling object,
838 *Int. J. Numer. Methods Fluids* 59 (2009) 91–115.
- 839 [42] G. Fourey, C. Hermange, D. L. Touzé, G. Oger, An efficient fsi coupling strat-
840 egy between Smoothed Particle Hydrodynamics and Finite Element methods,
841 *Comput. Phys. Commun.* 217 (2017) 66–81.
- 842 [43] M. S. Shadloo, G. Oger, D. Le Touzé, Smoothed particle hydrodynamics method
843 for fluid flows, towards industrial applications: Motivations, current state, and
844 challenges, *Comput. Fluids* 136 (2016) 11–34.
- 845 [44] A. J. C. Crespo, C. Altomare, J. M. Domínguez, J. González-Cao, M. Gómez-
846 Gesteira, Towards simulating floating offshore oscillating water column convert-
847 ers with Smoothed Particle Hydrodynamics, *Coast. Eng.* 126 (2017) 11–26.
- 848 [45] Z. Liu, Y. Wang, X. Hua, Numerical studies and proposal of design equations
849 on cylindrical oscillating wave surge converters under regular waves using SPH,
850 *Energy Convers. Manage.* 223 (2020) 112242.
- 851 [46] M. Brito, R. B. Canelas, O. Garcá-Feal, J. M. Domínguez, A. J. C. Crespo,
852 R. M. L. Ferreira, M. G. Neves, L. Teixeira, A numerical tool for modelling
853 oscillating wave surge converter with nonlinear mechanical constraints, *Renew.*
854 *Energy* 146 (2020) 2024–2043.
- 855 [47] P. Roperó-Giralda, A. J. Crespo, B. Tagliaferro, C. Altomare, J. M. Domínguez,
856 M. Gómez-Gesteira, G. Viccione, Efficiency and survivability analysis of a point-
857 absorber wave energy converter using DualSPHysics, *Renew. Energy* 162 (2020)
858 1763–1776.
- 859 [48] N. Quartier, A. J. C. Crespo, J. M. Domínguez, V. Stratigaki, P. Troch, Efficient
860 response of an onshore Oscillating Water Column Wave Energy Converter using
861 a one-phase SPH model coupled with a multiphysics library, *Appl. Ocean Res.*
862 115 (2021) 102856.

- 863 [49] G. R. Liu, M. B. Liu, Smoothed Particle Hydrodynamics, World Scientific, 2003.
- 864 [50] J. M. Domínguez, A. J. C. Crespo, M. Gómez-Gesteira, J. C. Marongiu, Neighbour
865 lists in smoothed particle hydrodynamics, *Int. J. Numer. Methods Fluids*
866 67 (2011) 2026–2042.
- 867 [51] H. Wendland, Piecewise polynomial, positive definite and compactly supported
868 radial functions of minimal degree, *Adv. Comput. Math.* 4 (1995) 389–396.
- 869 [52] J. J. Monaghan, Smoothed particle hydrodynamics, *Rep. Prog. Phys.* 68 (2005)
870 1703–1759.
- 871 [53] A. J. C. Crespo, Users Guide for DualSPHysics code, [https://github.com/
872 DualSPHysics/DualSPHysics/wiki](https://github.com/DualSPHysics/DualSPHysics/wiki) (2020).
- 873 [54] J. J. Monaghan, A. Kocharyan, SPH simulation of multi-phase flow, *Comput.*
874 *Phys. Commun.* 87 (1995) 225–235.
- 875 [55] A. Colagrossi, M. Antuono, D. Le Touzé, Theoretical considerations on the
876 free-surface role in the smoothed-particle-hydrodynamics model, *Phys. Rev. E*
877 79 (2009) 056701.
- 878 [56] A. Colagrossi, M. Antuono, D. Le Touzé, Theoretical analysis and numerical
879 verification of the consistency of viscous smoothed-particle-hydrodynamics for-
880 mulations in simulating free-surface flows, *Phys. Rev. E* 84 (2011) 026705.
- 881 [57] D. Molteni, A. Colagrossi, A simple procedure to improve the pressure evalu-
882 ation in hydrodynamic context using the SPH, *Comput. Phys. Commun.* 180
883 (2009) 861–872.
- 884 [58] M. Antuono, A. Colagrossi, S. Marrone, D. Molteni, Free-surface flows solved
885 by means of SPH schemes with numerical diffusive terms, *Comput. Phys. Com-
886 mun.* 181 (2010) 532–549.
- 887 [59] J. J. Monaghan, Smoothed particle hydrodynamics, *Annu. Rev. Astron. Astro-
888 phys.* 30 (1992) 543–574.
- 889 [60] M. S. Shadloo, R. Weiss, M. Yildiz, R. A. Dalrymple, Numerical simulation of
890 long wave run-up for breaking and non-breaking waves, *Int. J. Offshore Polar*
891 25 (2015) 1–7.
- 892 [61] J. J. Monaghan, K. A., Solitary waves on a cretan beach, *J. Waterway, Port,
893 Coastal, Ocean Eng.* 125 (1999) 145–154.

- 894 [62] S. J. Lind, R. Xu, P. K. Stansby, B. D. Rogers, Incompressible smoothed par-
895 ticle hydrodynamics for free-surface flows: A generalised diffusion-based algo-
896 rithm for stability and validations for impulsive flows and propagating waves,
897 *J. Comput. Phys.* 231 (2012) 1499–1523.
- 898 [63] R. A. Dalrymple, O. Knio, SPH modelling of water waves, in: *Coastal Dynam-*
899 *ics'01*, 2001, pp. 779–787.
- 900 [64] A. J. C. Crespo, M. Gómez-Gesteira, R. A. Dalrymple, Boundary conditions
901 generated by dynamic particles in SPH methods, *Comput. Mater. Contin.* 5
902 (2007) 173–184.
- 903 [65] R. B. C. Canelas, A. J. C. Crespo, M. Brito, J. M. Domínguez, O. García-Feal,
904 Extending DualSPHysics with a differential variational inequality: modeling
905 fluid-mechanism interaction, *Appl. Ocean Res.* 76 (2018) 88–97.
- 906 [66] O. S. Madsen, On the generation of long waves, *J. Geophys. Res.* 76 (1971)
907 8672–8683.
- 908 [67] I. Zabala, J. Henriques, J. Blanco, A. Gomez, L. Gato, I. Bidaguren, A. Falcão,
909 A. Amezaga, R. Gomes, Wave-induced real-fluid effects in marine energy con-
910 verters: review and application to OWC devices, *Renew. Sustain. Energy Rev.*
911 111 (2019) 535–549.
- 912 [68] S. Dai, S. Day, Z. Yuan, H. Wang, Investigation on the hydrodynamic scaling ef-
913 fect of an OWC type wave energy device using experiment and CFD simulation,
914 *Renew. Energy* 142 (2019) 184–194.
- 915 [69] A. Babarit, H. J. Todalshaug, On the maximum and actual capture width ratio
916 of wave energy converters, in: *Proceedings of the 9th European Wave and Tidal*
917 *Energy Conference*, 2011, pp. 1–18.
- 918 [70] X. Garnaud, C. C. Mei, Comparison of wave power extraction by a compact
919 array of small buoys and by a large buoy, in: *Proceedings of the 8th European*
920 *Wave and Tidal Energy Conference*, 2009, pp. 934–942.
- 921 [71] X. Garnaud, C. C. Mei, Wave-power extraction by a compact array of buoys, *J.*
922 *Fluid Mech.* 635 (2009) 389–413.